Journal of
METAMORPHIC GEOLOGY

J. metamorphic Geol., 2011 doi:10.1111/j.1525-1314.2011.00945.x

Microstructural evidence for magma confluence and reusage of magma pathways: implications for magma hybridization, Karakoram Shear Zone in NW India

P. HASALOVÁ,[1] R. F. WEINBERG[1] AND C. MACRAE[2]
[1]*School of Geosciences, Monash University, Clayton, Vic. 3800, Australia (pavlina.hasalova@monash.edu)*
[2]*Microbeam Laboratory, CSIRO, Process Science and Engineering, Clayton, Vic. 3186, Australia*

ABSTRACT In the Karakoram Shear Zone, Ladakh, NW India, Miocene leucogranitic dykes form an extensive, varied and complex network, linking an anatectic terrane exposed in the Pangong Range, with leucogranites of the Karakoram Batholith. Mineral paragenesis of the heterogeneous anatectic source rocks suggests melting has resulted from water influx into rocks at upper amphibolite facies conditions, and microstructures suggest anatexis was contemporaneous with shearing. The network is characterized by continuous and interconnected dykes, with only rare cross-cutting relationships, forming swarms and chaotic injection complexes where magmatic rocks cover up to 50% of the outcrop area. Despite this volume of magma, the system did not lose continuity, suggesting that it did not flow *en masse* and that the magma network was not all liquid simultaneously. Leucogranites in this network, including leucosomes in migmatites, carry an isotopic signature intermediate between the two main anatectic rocks in the source, suggesting efficient homogenization of the magmatic products. Here, we describe a number of microscopic features of these magmatic rocks which suggests that several pulses of magma used the same pathways giving rise to textural and chemical disequilibrium features. These include: (i) narrow, tortuous corridors of fine-grained minerals cutting across or lining the boundaries of larger grains, interpreted to be remnants of magma-filled cracks cutting across a pre-existing magmatic rock; (ii) corrosion of early formed grains at the contact with fine-grained material; (iii) compositional zoning of early formed plagioclase and K-feldspar grains and quartz overgrowths documented by cathodoluminescence imaging; (iv) incipient development of rapakivi and anti-rapakivi textures, and (iv) different crystallographic preferred orientation of early formed quartz and fine-grained quartz. Mapping of the fine-grained corridors interpreted to represent late melt channels reveal an interlinked network broadly following the S-C fabric defined by pre-existing magmatic grains. We conclude that early formed dykes provided a pathway exploited intermittently or continuously by new magma batches. New influxes of magma opened narrow channels and migrated through a microscopic network following predominantly grain boundaries along an S-C fabric related to syn-magmatic shearing. A mixed isotopic signature resulted not from the mixing of magmas, but from the micro-scale interaction between new magma batches and previously crystallized magmatic rocks, through local equilibration.

Key words: Himalayan leucogranites; magma mixing; magma pathways; melt; migmatite.

INTRODUCTION

Numerous plutons and batholiths have hybrid signatures between those of the mantle and crust (e.g. Kistler, 1974; Reid *et al.*, 1983; DePaolo *et al.*, 1992; Poli, 1992; Kerr & Fryer, 1993; Soesoo & Nicholls, 1999; Gagnevin *et al.*, 2004). These are commonly interpreted to result from either mixing between magmas from mantle and crustal sources (e.g. Crawford & Searle, 1992), or from assimilation of crustal rocks by hot mantle magmas (e.g. Kerr *et al.*, 1995; Reiners *et al.*, 1995; Beard *et al.*, 2005). Just how this happens is unclear. Mixing of magmas from different sources is inhibited by differences in physical properties (Huppert & Sparks, 1988), and crustal assimilation is limited by the thermal budget of the intruding mantle magmas and must in part rely on physical disaggregation of country rocks (Grove *et al.*, 1988; Green, 1994; Clarke *et al.*, 1998).

Efficient mechanisms of magma hybridization must exist in order to explain the abundance of hybridized magmatic rocks in continents. This paper focuses on two intertwined questions: how do magmas migrate and how do they develop a hybrid signature. We focus on the magma source and transfer terrane exposed in the Pangong Range, within the 10 km wide Karakoram Shear Zone in Ladakh, NW India. Anatexis is temporally, chemically and geographically related to the Miocene Karakoram (or Baltoro) Batholith (Srimal, 1986; Parrish & Tirrul, 1989; Crawford &

Windley, 1990; Searle *et al.*, 1998; Phillips *et al.*, 2004; Mahéo *et al.*, 2009; Weinberg *et al.*, 2009; Reichardt *et al.*, 2010).

A number of magma mixing scenarios have been proposed to explain the isotopic signature of this batholith, such as the generation of melt from a metasomatized mantle (evidenced by exposed lamprophyres) and its mixing with crustal magmas generated by heat advected into the crust (Mahéo *et al.*, 2009). In a study of the anatectic rocks within the Pangong Range, Reichardt *et al.* (2010) demonstrated that the hybrid signature of the Miocene magmatic rocks is similar to those found in leucosomes, and derived from the contemporaneous melting of interlayered crustal rocks with different isotopic signatures, and their subsequent hybridization. They found that even *in source* leucosomes have hybrid signatures, and argued that mixing must have occurred already in the source along magma extraction pathways.

This work is expanded here by investigating in detail petrographic features of these Miocene magmatic rocks in the source and transfer network. Microstructural observations reveal narrow, tortuous corridors of fine-grained granitic material cutting across or lining the boundaries of larger grains. These corridors link together and form an interconnected network and are accompanied by textural and chemical disequilibrium features. A number of possible ways in which these microstructures may have formed are discussed, including: solid-state deformation, continuous melt crystallization in a closed system, and sub-solidus hydrothermal alteration, and it is concluded that they most likely represent intrusive channelways of new magma batches into previously crystallized magmas. We argue that the leucogranitic rocks are a result of the reaction between early crystallized material and new injections, leading to the hybrid isotopic signature. The paper starts with a brief overview of the migmatites of the Pangong Range, including their field relationships, metamorphic conditions during anatexis, and isotopic signature of magmatic rocks and source rocks. It then proceeds to present the textural evidence indicative of this process.

PANGONG RANGE: ANATECTIC TERRANE

The Pangong Range is an exhumed wedge of rocks in between two strands of the Karakoram Shear Zone (Fig. 1; Weinberg *et al.*, 2000; McCarthy & Weinberg, 2010). Its rocks and relationships with the Karakoram Shear Zone have been described by a number of authors (e.g. Searle *et al.*, 1998; Weinberg & Searle, 1998; Rolland & Pêcher, 2001; Lacassin *et al.*, 2004; Phillips *et al.*, 2004; Rutter *et al.*, 2007; Searle & Phillips, 2007; Weinberg & Mark, 2008; Rolland *et al.*, 2009; Weinberg *et al.*, 2009; Reichardt *et al.*, 2010). The range comprises the Pangong Metamorphic Complex which includes the Cretaceous calcalkaline Muglib Batholith (72–70 Ma; Ravikant, 2006; Reichardt *et al.*, 2010) intruded into volcano-sedimentary rocks (Fig. 1), now represented by a sequence of metasedimentary rocks including biotite-rich psammites, semipelites and pelites, and hornblende-bearing rocks such as gneisses and amphibolites, interlayered with bands of calcsilicates, varying in size from narrow, disrupted bands to lenses several hundred metres wide (Weinberg & Mark, 2008).

In the Pangong Range, the metasedimentary rocks and the *c.* 70 Ma calcalkaline granitoids intruding them, have all undergone partial melting forming migmatites linked to and intruded by leucogranitic dykes and irregular pods, stocks and plutons from hundreds of metres to a kilometre wide (Fig. 2; Weinberg & Searle, 1998; Weinberg & Mark, 2008; Weinberg *et al.*, 2009). Anatectic products range from leucotonalites to leucogranites (Reichardt *et al.*, 2010). The term leucogranite is used henceforth in *sensu lato* to refer to this group of rocks.

Extensive anatexis occurred in upper amphibolite facies conditions estimated at 700 ± 20 °C at 7 kbar (Rolland *et al.*, 2009) or 700–750 °C at 4–5 kbar (Rolland & Pêcher, 2001) and leucogranitic rocks crystallized between 20 and 13.5 Ma (U–Pb zircon; Searle *et al.*, 1998; Phillips *et al.*, 2004; Reichardt *et al.*, 2010). The older ages of this range are interpreted to date the timing of anatexis, and the younger ages to represent intrusive rocks that might not necessarily reflect *in situ* melting.

Reichardt *et al.* (2010) demonstrated that hybridization of magmas in this system occurred already in the source. The calcalkaline granitoids have a juvenile isotopic signature with small crustal influence (initial $^{87}Sr/^{86}Sr$ = 0.7042–0.7077 and ε_{Nd} = +0.6 to +2.4; Fig. 3), in contrast to the metasedimentary rocks which have a distinctly crustal signature (initial $^{87}Sr/^{86}Sr$ = 0.7115–0.7161 and ε_{Nd} = −10.0 to −9.6; Fig. 3). Leucogranitic veins, dykes and larger bodies derived from anatexis of these two rock sequences were found to have a hybrid signature (initial $^{87}Sr/^{86}Sr$ = 0.7076–0.7121 and ε_{Nd} = −3.6 to −7.1; Fig. 3), including, surprisingly, leucosomes interpreted to be still roughly *in situ*. Thus, Reichardt *et al.* (2010) concluded that hybridization had already occurred in the leucosomes still in the source, and that it was likely to be a result of magma from different sources flowing through the same magma network, for which they presented outcrop scale examples. Here, we investigate the textures of these leucosomes and leucogranite intrusions and describe features interpreted to represent reopening and reusage of magma pathways.

MAGMA PATHWAYS: AN INTERCONNECTED NETWORK

The leucogranitic rocks that resulted from Miocene anatexis form a complex and interconnected network of leucosomes, dykes, irregular sheets, pods, stocks and plutons (Fig. 2; Weinberg & Regenauer-Lieb,

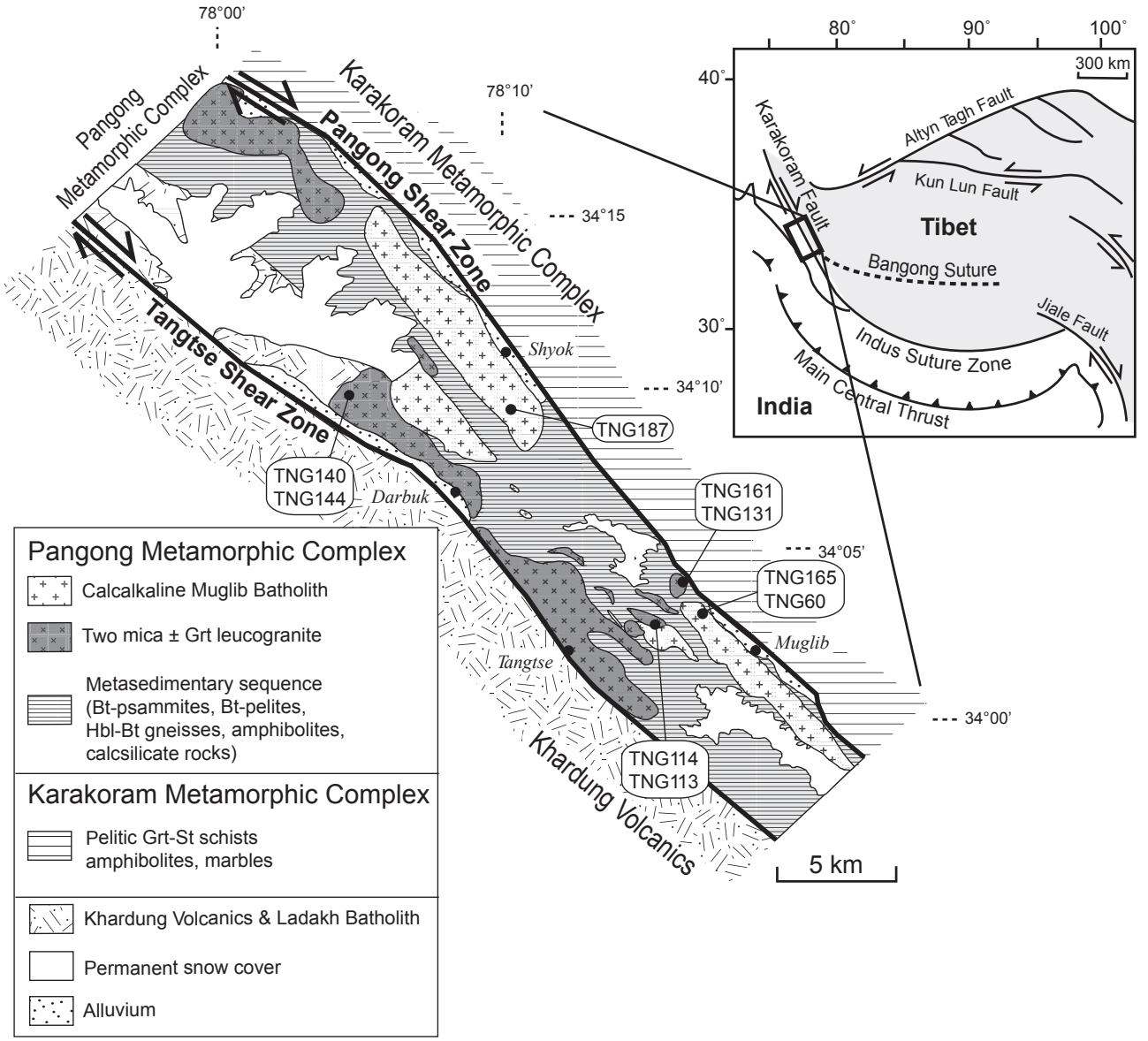

Fig. 1. Geological map of the Pangong Range and bordering units within the Karakoram Shear Zone. The Karakoram Shear Zone splits here into two strands, the Pangong and Tangtse Shear Zones, bounding the Pangong Metamorphic Complex and the Pangong Range (modified after Reichardt *et al*., 2010). Location of studied samples is indicated. Inset box shows general location of the Pangong Range within the Himalaya-Tibet region.

2010; Reichardt & Weinberg, in press). The key feature of this network is that magmatic structures commonly merge seamlessly, with relatively rare cross-cutting relationships or relative displacement (Fig. 2). The network of leucosomes in stromatic migmatites is comprised of sheets oriented parallel to layering interconnected with sheets parallel to the axial planes of folds (Weinberg & Mark, 2008). Stromatic migmatites are disrupted to form patches of diatexite that vary in size from a few to hundreds of metres (Reichardt & Weinberg, in press). The transition from leucosomes in migmatites to larger magma sheets is gradual, forming injection complexes and a hierarchy of magma channels that feed into stocks and plutons and ultimately into the Karakoram Batholith (Weinberg & Searle, 1998; Weinberg *et al*., 2009; Reichardt *et al*., 2010; Reichardt & Weinberg, in press).

Some outcrops preserve evidence of the confluence of magmas from different sources (Reichardt *et al*., 2010). One example is the confluence of intrusive pegmatitic Bt + Ms + Grt leucogranite dykes with *in situ* hornblende-bearing leucosomes with an irregular and diffusive margin against calcalkaline granitoid source. Both in the field and in thin section the contact in this example is seamless and the isotopic signature of the resulting granitic rocks is hybrid ($^{87}Sr/^{86}Sr$ = 0.7087 and ε_{Nd} = −4.5; Reichardt *et al*., 2010). Another example is leucosome from

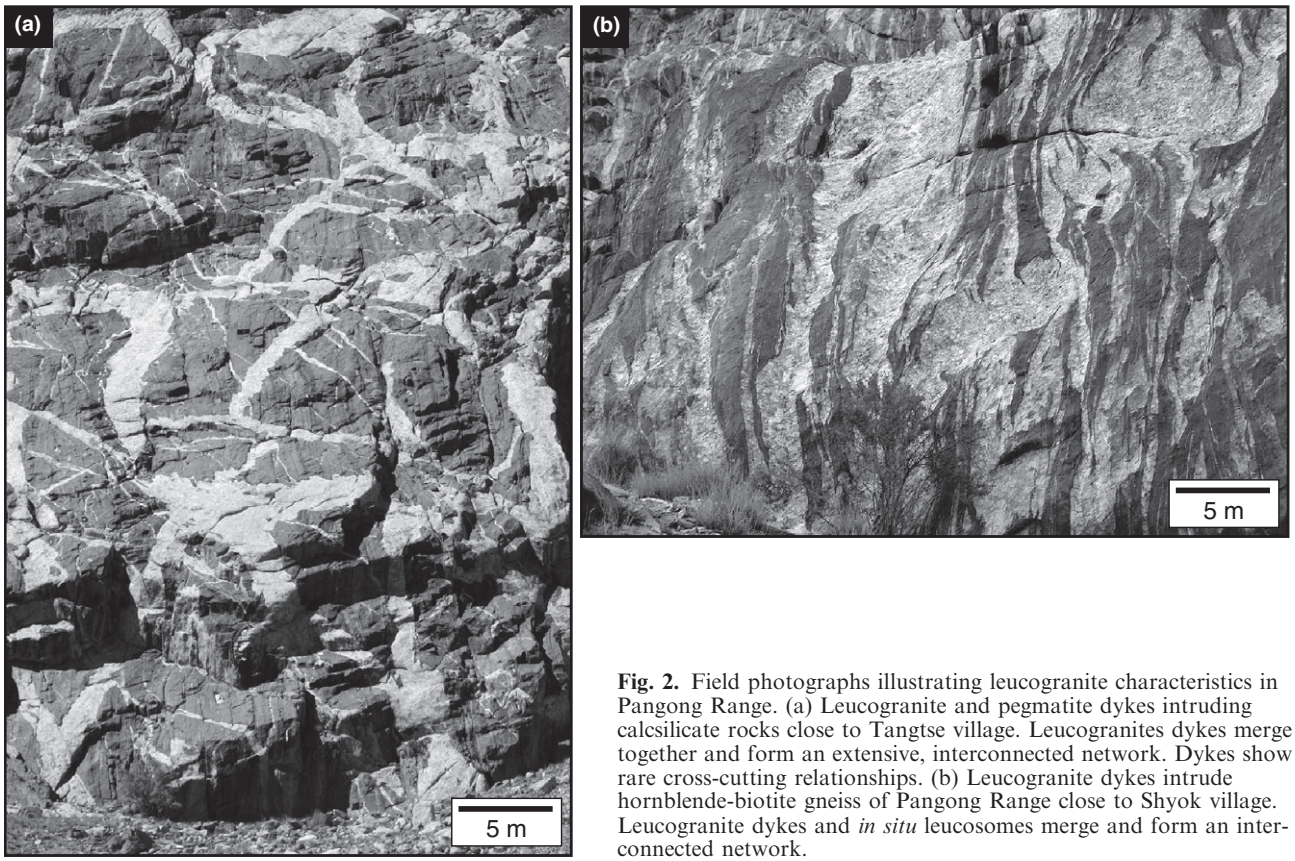

Fig. 2. Field photographs illustrating leucogranite characteristics in Pangong Range. (a) Leucogranite and pegmatite dykes intruding calcsilicate rocks close to Tangtse village. Leucogranites dykes merge together and form an extensive, interconnected network. Dykes show rare cross-cutting relationships. (b) Leucogranite dykes intrude hornblende-biotite gneiss of Pangong Range close to Shyok village. Leucogranite dykes and *in situ* leucosomes merge and form an interconnected network.

a calcalkaline granodiorite intruding into meta-psammites. This leucosome contains garnet from the country rock, and has a hybrid isotopic signature ($^{87}Sr/^{86}Sr = 0.7088$ and $\varepsilon_{Nd} = -3.6$; Reichardt *et al.*, 2010).

LEUCOSOME AND GRANITIC DYKE PETROGRAPHY

Rocks in leucosomes and dykes have compositions ranging from leucogranite to leucotonalite. All these leucogranitic rocks are derived from the two main protoliths, either from partial melting of calcalkaline granitoids (comprised Qtz + Pl + Kfs + Bt + Hbl ± Cpx ± Ttn) or metasedimentary rocks (comprised Qtz + Pl + Bt ± Grt ± Ms). Two major leucosome types have been distinguished: (i) hornblende-bearing leucosomes related to anatexis of hornblende-bearing calcalkaline magmatic rocks (Fig. 4a,b; Table 1; e.g. sample TNG165) and (ii) two mica-bearing leucosomes related to anatexis of the biotite-rich psammites (Fig. 4c; Table 1; e.g. TNG131E).

Hornblende-bearing leucosomes (Fig. 4a,b) vary in composition from granite to granodiorite. They are derived from calcalkaline granitoids and typically have the assemblage Kfs + Pl + Qtz + Hbl + Ttn + Ap ± Bt ± Ms ± Zrn ± Mnz (Table 1). Hornblende is interpreted to be peritectic and forms large euhedral to anhedral poikilitic grains (0.1–0.5 mm) that are associated with euhedral titanite and including small quartz, apatite and biotite grains (Fig. 4b). Apatite, zircon and monazite are accessory phases. Growth of the peritectic hornblende associated with titanite in these leucosomes could be explained by the presence of water during metamorphism (e.g. Mogk, 1992; Gardien *et al.*, 2000; Berger *et al.*, 2008; Reichardt *et al.*, 2010).

Two mica-bearing leucosomes (Fig. 4c) are derived from partial melting of biotite-rich psammites and their composition ranges from granite to tonalite. The mineral assemblage is Pl + Qtz + Kfs + Bt + Ms + Grt ± Zrc ± Mnz ± Ap ± Aln ± Ilm (Fig. 4c; Table 1). Leucosomes and melanosomes typically lack peritectic minerals that would support biotite dehydration melting (e.g. Thompson, 1982; White *et al.*, 2007). Rare atoll-shaped garnet (0.1–0.5 mm in size; < 0.5 mol.%) is present; however, it is distributed randomly throughout the whole rock without any obvious relation to leucosomes or melanosome. Apatite, zircon, monazite and ilmenite are present as accessory phases (Table 1). All these observations support extensive H_2O-fluxed melting of both, metasedimentary and calcalkaline igneous protoliths (Weinberg & Mark, 2008; Reichardt *et al.*, 2010). This is also consistent with peak metamorphic conditions for Miocene anatexis estimated for this exposed section at

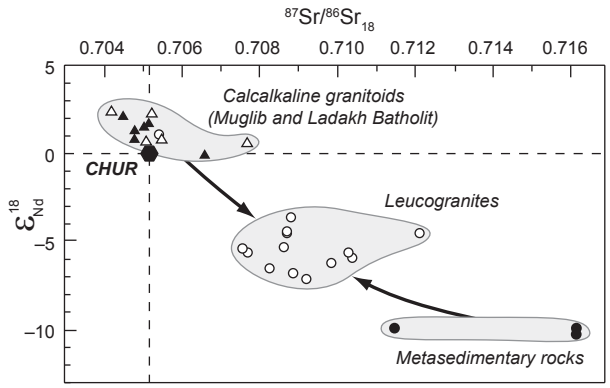

Fig. 3. Sr-Nd isotopic compositions for source rocks and leucogranites, including leucosome samples (data from Reichardt *et al*., 2010). $^{87}Sr/^{86}Sr_{18}$ and ε^{18}_{Nd} values (calculated for initial age of 18 Ma) are distinct for both of the main magma sources: calcalkaline granitoids (Muglib Batholith = open triangles) and metasedimentary rocks (black circles). Anatectic products (open circles) have intermediate values and can be modelled by mixing of both source rocks (Reichardt *et al*., 2010). Also plotted for comparison are the values for samples from the Ladakh Batholith, south of the Karakoram Fault (black triangles).

upper amphibolite conditions (Rolland & Pêcher, 2001; Rolland *et al*., 2009), too low to cause widespread melting without considering external water influx.

MICROSTRUCTURAL OBSERVATIONS

Detailed microstructural work has been done in order to describe melt distribution and topology in leucosomes and dykes at microscale. Thin sections were cut perpendicular to the foliation and parallel to lineation (XZ section). Fourteen representative leucosomes and dykes samples (Table 1) were mapped in detail using optical microscope and backscattered electron (BSE) images. Backscattered electron images were collected using the SEM Philips XL30 ESEM with attached Oxford Inca EDX microanalytical system at the University of Melbourne, Australia, at 20 kV acceleration voltage. Mineral compositions were analysed using the Cameca SX50 at the University of Melbourne in point beam mode at 15 kV acceleration voltage and 35 nA beam current. Compositional maps of plagioclase and K-feldspar grains were obtained using the JEOL 8500F HyperProbe with twin Bruker silicon drift detectors at the CSIRO, Process Science and Engineering, Melbourne, Australia, at 20 kV acceleration voltage and 40 nA beam current. Representative mineral analyses are summarized in Table 2.

Leucosome and dyke textures

Both granitic rock types (hornblende- and two mica-bearing) are medium to coarse grained and consist dominantly of plagioclase, K-feldspar and quartz in different proportions (> 95 modal%). These minerals have two distinct appearances. They either form large,

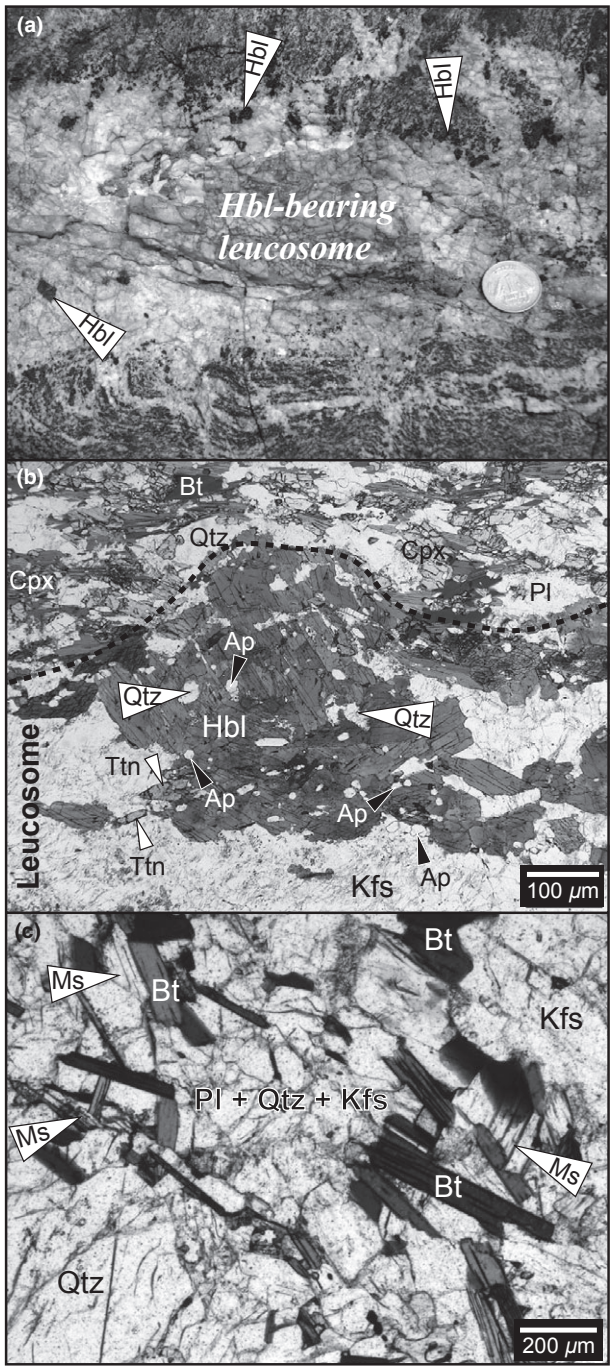

Fig. 4. Field photograph and photomicrographs showing typical mineral assemblages in two main leucosome types. (a, b) Hornblende-bearing leucosome as a result of *in situ* H_2O-fluxed partial melting of diorite. (a) *In situ* leucosome contains large (up to 1 cm) peritectic hornblende crystals and has irregular boundaries against diorite of the Muglib Batholith. (b) Leucosome has a granitic composition with euhedral, poikilitic hornblende that includes apatite, quartz and biotite grains (sample TNG165). Titanite is spatially related to hornblende. (c) Two mica-bearing leucosome derived from melting of biotite-rich psammites (sample TNG144). Leucosome has granitic composition with euhedral biotite and muscovite grains. No peritectic minerals are present.

Table 1. Summary description of samples investigated here. Abbreviations after Kretz (1983). Location of samples shown in Fig. 1.

Sample	Coordinates		Rock type	Mineralogy
	Latitude	Longitude		
TNG60A	34°03′25.3″N	78°14′13.3″E	Hbl-bearing leucosome	Kfs + Qtz + Pl + Hbl ± Bt ± Ep ± Ttn ± Ap ± Zrn
TNG60C	34°03′25.3″N	78°14′13.3″E	Hbl-bearing leucosome	Kfs + Qtz + Pl + Hbl + Bt + Ttn + Ep ± Ap ± Zrn ± Mnz ± Aln
TNG60D	34°03′25.3″N	78°14′13.3″E	Hbl-bearing leucosome	Kfs + Qtz + Pl + Hbl ± Bt ± Ttn ± Tur ± Ap ± Zrn ± Aln
TNG114	34°02′35.2″N	78°13′22.5″E	Hbl-bearing leucosome	Kfs + Qtz + Pl + Hbl + Bt ± Ms ± Zrn ± Ap
TNG165	34°03′25.3″N	78°14′13.3″E	Hbl-bearing leucosome	Kfs + Qtz ± Pl + Hbl + Bt ± Ttn ± Ap ± Ms ± Zrn ± Mnz
TNG113A	34°02′35.0″N	78°13′23.0″E	Hbl-bearing leucosome	Kfs + Qtz + Pl ± Ttn ± Hbl ± Bt ± Chl ± Ap ± Zrn
TNG113I	34°02′35.0″N	78°13′23.0″E	Two mica-bearing leucosome	Kfs + Qtz + Pl + Bt + Ms ± Chl ± Zrn ± Mnz ± Aln
TNG131E	34°03′38.8″N	78°13′52.1″E	Two mica-bearing leucosome	Kfs + Qtz + Pl + Bt + Ms ± Ap ± Grt ± Ilm
TNG131F	34°03′38.8″N	78°13′52.1″E	Two mica-bearing leucosome	Kfs + Qtz + Pl + Bt ± Ms ± Zrn ± Ilm ± Aln
TNG144	34°09′54.1″N	78°03′34.7″E	Leucogranite dyke	Kfs + Qtz + Pl + Ms + Bt ± Zrn ± Mnz
TNG140	34°09′45.9″N	78°03′26.0″E	Leucogranite dyke	Kfs + Qtz + Pl ± Ms ± Bt ± Zrn ± Mnz
TNG161A	34°03′57.7″N	78°13′37.2″E	Leucogranite dyke	Kfs + Qtz + Pl ± Grt ± Bt ± Ms ± Zrn
TNG187A	34°08′48.6″N	78°08′26.9″E	Leucogranite dyke	Kfs + Qtz + Pl ± Grt ± Bt ± Zrn
TNG187B	34°08′48.6″N	78°08′26.9″E	Leucogranite dyke	Kfs + Qtz + Pl ± Tur ± Grt ± Bt ± Ttn ± Zrn

Kfs, K-feldspar; Qtz, quartz; Pl, plagioclase; Hbl, hornblende; Bt, biotite; Ms, muscovite; Ep, epidote; Ttn, titanite; Tur, tourmaline; Ap, apatite; Zrn, zircon; Mnz, monazite; Grt, garnet; Chl, chlorite; Aln, allanite; Ilm, ilmenite.

irregular grains or small to medium-sized interstitial grains (Fig. 5). The large K-feldspar, plagioclase and quartz grains have grain size range of 0.1–5 mm, with average grain size of 0.5–0.9 mm. In contrast, small interstitial grains have a significantly smaller average grain size of 0.2–0.5 mm, with wide grain size range of 20μm–2 mm (Figs 5 & 6).

Relationships between fine and coarse-grained regions

Fine-grained material of granitic composition forms irregular but continuous bands of different and varying widths. The distribution of these bands in leucosomes and dykes is heterogeneous and, based on width, three distinct textural appearances have been identified (Fig. 5). (i) Narrow corridors (< 100 μm wide) of fine-grained material of plagioclase, K-feldspar and quartz and minor apatite coating large grain boundaries or cutting across them (Fig. 5a,b). These narrow corridors extend for the length of a single or a few large grains and tend to form short, linked arrays around and through large crystals. They tend to be preferentially oriented parallel to the dominant foliations defined by the preferred orientation of the large crystals, or to a secondary foliation at an angle of 45° to the dominant one (Fig. 6a). (ii) Wider corridors (100–500 μm wide; Fig. 5c,d) comprise aggregates of plagioclase, K-feldspar and quartz that either form a well-equilibrated mosaic of grains with straight boundaries and convex shapes, or coat large crystals of K-feldspar, plagioclase

Table 2. Representative analyses of plagioclase and K-feldspar.

Mineral	Plagioclase								K-feldspar		
Microstructure	Palaeo-crystals		Neo-crystals						Palaeo-crystals		Neo-crystals
			Narrow films		Corridor		Wide bands				
Position	Core	Rim	Core	Rim	Core	Rim	Centre	Margin	Core	Rim	
Sample	TNG165		TNG165		TNG165		TNG165		TNG165		TNG165
Wt% oxide											
SiO_2	61.86	68.74	67.39	65.58	65.86	67.04	63.68	64.97	64.58	65.00	63.90
Al_2O_3	24.15	19.59	20.18	20.55	21.28	21.96	22.55	22.05	18.95	18.32	18.98
CaO	4.99	0.14	0.54	0.00	1.87	0.00	3.90	3.09	0.06	0.04	0.05
Na_2O	8.84	11.74	11.67	13.70	10.84	11.32	9.76	10.26	1.95	1.30	1.21
K_2O	0.31	0.37	0.13	0.17	0.14	0.24	0.23	0.18	14.01	15.30	15.65
Total	100.15	100.58	99.91	100.00	99.99	100.56	100.12	100.55	99.55	99.96	99.79
Cations/Charges	5/16	5/16	5/16	5/16	5/16	5/16	5/16	5/16	5/16	5/16	5/16
Si	2.73	2.98	2.94	2.81	2.88	2.91	2.80	2.84	2.97	2.99	2.94
Al	1.26	1.00	1.03	1.04	1.10	1.12	1.17	1.13	1.03	0.99	1.03
Ca	0.24	0.01	0.03	0.00	0.09	0.00	0.18	0.14	0.00	0.00	0.00
Na	0.76	0.99	0.99	1.14	0.92	0.95	0.83	0.87	0.17	0.17	0.11
K	0.02	0.02	0.01	0.01	0.01	0.01	0.01	0.01	0.82	0.89	0.92
Total	5.0	5.0	5.0	5.0	5.0	5.0	5.0	5.0	5.0	5.0	5.0
End-members											
Ab	0.749	0.973	0.968	0.992	0.906	0.986	0.809	0.849	0.001	0.000	0.002
An	0.234	0.006	0.025	0.000	0.086	0.000	0.179	0.141	0.171	0.160	0.105
Or	0.017	0.020	0.007	0.008	0.008	0.014	0.013	0.010	0.828	0.840	0.893

An = Ca/(Ca + Na + K); Ab = Na/(Ca + Na + K); Or = K/(Ca + Na + K).

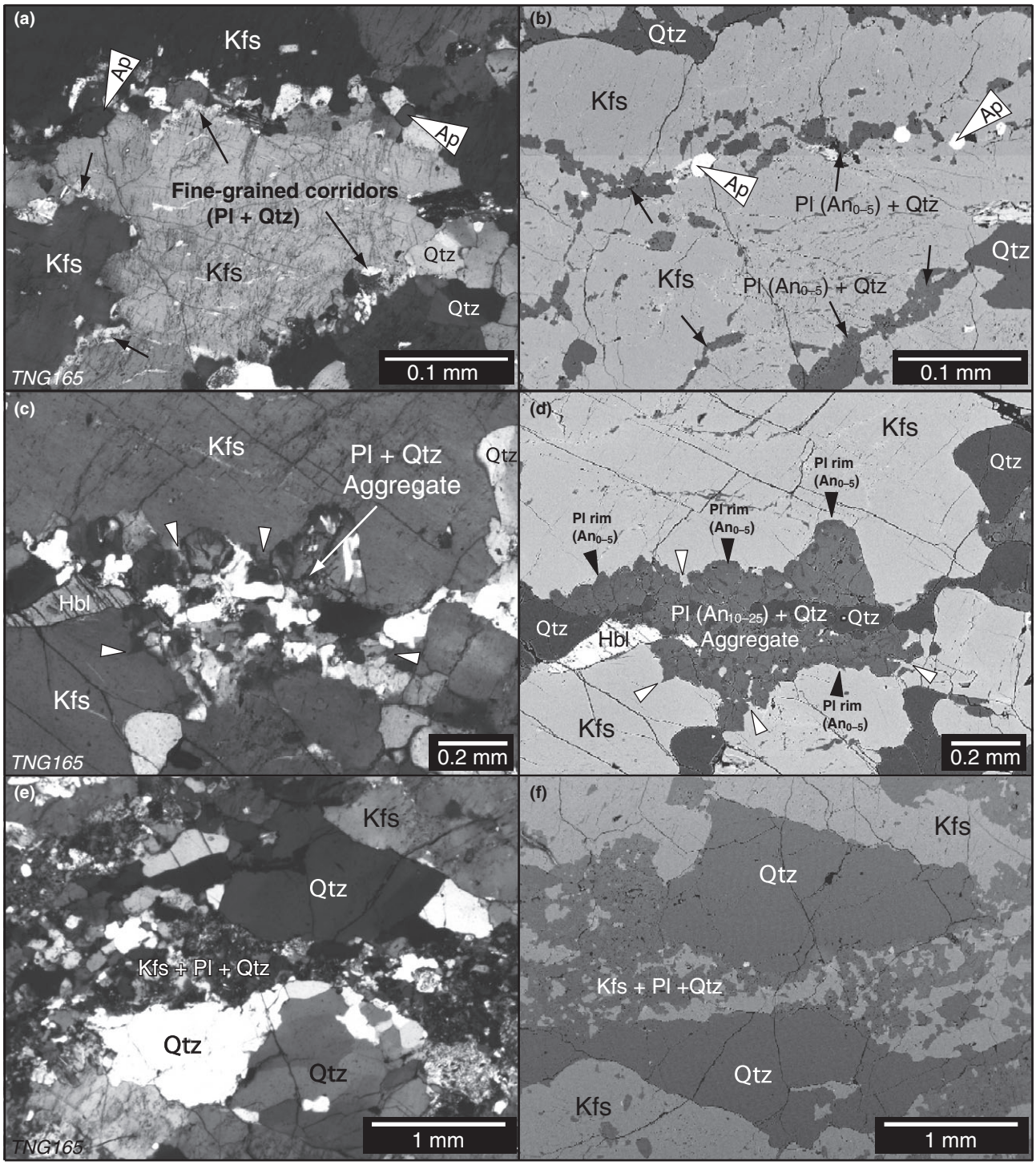

Fig. 5. Photomicrographs (left) and backscattered electron images (right) showing distinct appearance and width of fine-grained bands (sample TNG165). Images show corridors of fine-grained plagioclase, K-feldspar and quartz in coarse-grained surrounding, increasing in width from (a) to (f). (a, b) Narrow corridors of fine-grained material ($<$ 100 μm wide; black arrows) along most of large grain boundaries. Apatite is spatially related to these thin corridors. (c, d) Wider, irregular aggregate of fine- to medium-grained material (100–500 μm wide) cross-cutting large K-feldspar grain in optical continuity on both sides of the fine-grained corridor. Fine-grained plagioclase shows normal zoning with $An_{10–25}$ in core and distinct albitic rims ($An_{0–5}$; black arrows). Both, fine-grained plagioclase and quartz grains are texturally equilibrated with straight boundaries and convex shapes. Locally, large K-feldspar grains have corroded shapes (white arrows). (e, f) Wide bands of fine-grained material ($>$ 0.5 mm wide) cut across coarse-grained quartz grains.

and quartz. (iii) Large bands (> 0.5 mm wide) of plagioclase, K-feldspar and quartz grains cross-cutting large grains (Fig. 5e,f) forming an extensive network predominantly oriented parallel or sub-parallel to foliation (Fig. 6b). These continuous or semi-continuous fine-grained granitic tracks link together and form an extensive network branching around large grains (Fig. 6). The large grains are not simply isolated phenocrysts in a groundmass of fine-textured crystals, they are either large single crystals or aggregates of all three felsic phases, representing granitic composition (e.g. in Figs 5–7) with many of their grain boundaries coated by fine-grained granitic material, or a number of large grains cut across by tortuous corridors of fine-grained minerals.

Fine-grained bands range from ~5–10 to ~80 vol.% of the rock (Fig. 6). Increase in the proportion of fine-grained material is accompanied by the widening of the corridors, increased grain size and increased corrosion of coarse-grain aggregates in between the bands. The net effect is that with increasing modal proportion of fines, the distinction between the two components becomes increasingly blurred because of the development of grain-size gradation. Microstructural characteristics of the coarse- and fine-grained rock-forming minerals are described separately.

Microstructural characteristics of coarse grains

K-feldspar grains are not visibly plastically deformed, but are preferentially oriented parallel to foliation. They form large irregularly shaped grains (0.5–1 mm in size) with embayed, high-energy boundaries (Fig. 7a–e), mostly traced or cross-cut by the fine-grained interstitial material (comprised of plagioclase and quartz; e.g. Fig. 5a,b). Commonly, the number of embayments correlates with amount of fine-grained material (Fig. 7a–e). K-feldspar shape varies from slightly embayed corresponding to small irregular embayments filled with quartz and plagioclase (Fig. 7a,b), to highly irregular corroded relicts of larger grains (Fig. 7c). It is common to find in these rocks extreme cases of resorption of large grains of K-feldspar represented by skeletal-like, optically continuous relicts (Fig. 7d,e). K-feldspar boundaries not decorated by fine-grained material are straight to slightly lobate. Fine myrmekitic aggregates and perthite exsolution are common along K-feldspar boundaries (Figs 7a & 8a–c). Single, large K-feldspar grains are traversed by irregular tracks of fine-grained material with irregular margins (Figs 5b & 8). K-feldspar grains are orthoclase and exhibit clear zoning with more potassic rims at boundaries lined with fine-grained material (Fig. 9a; Table 2). Plagioclase inclusions in K-feldspar have oligoclase cores surrounded by albitic rims (Fig. 7b).

Plagioclase forms large irregular, commonly twinned grains (0.3–0.8 mm). Like K-feldspar, it is not visibly plastically deformed, and generally is preferentially oriented parallel to foliation. Coarse grains are traced by fine-grained K-feldspar and quartz, but not plagioclase (Fig. 7f,g). Plagioclase shows embayed, high-energy boundaries (Fig. 7f,g), but with less pronounced curvature than corroded coarse K-feldspar grains. Plagioclase grains in direct contact with other large grains have straight to slightly lobate boundaries. The grains are generally oligoclase and have normal zoning (core = $An_{15–25}$; rim = $An_{5–10}$) at boundaries lined with fine-grained material (Table 2). Plagioclase grains are also traversed by irregular trails of fine-grained material (Fig. 7f,g) and do not contain inclusions.

Quartz forms large (0.7–1.0 mm), irregular, weakly deformed grains, showing wavy undulatory extinction, and straight to lobate boundaries (Figs 5e,f & 7h). The boundaries of most large quartz grains are traced by fine-grained K-feldspar and plagioclase, but not quartz (Figs 5e,f & 7h). Quartz is also traversed by narrow corridors of fine-grained material, but does not contain isolated inclusions.

In summary, coarse-grained crystals of quartz, plagioclase or K-feldspar are cross-cut or part surrounded by fine-grained granitic material. Contacts with the fine grains are typically corroded and irregular, and except for the undulatory extinction in quartz, large grains are not obviously deformed.

Microstructural characteristics of fine grains

The fine grained, irregular and tortuous bands of plagioclase, K-feldspar and quartz occur along grain boundaries or cut across large crystals (Fig. 8). Fine-grained feldspar and quartz range in size from ~10 to 50 μm in thin films up to ~200 μm in corridors and up to 2 mm in wide bands. Fine interstitial plagioclase and K-feldspar grains have preferentially elongated shapes with low dihedral angles against coarse quartz and feldspar grains. Quartz, in contrast, forms small interstitial rounded shapes with high dihedral angles against feldspar. Feldspar and quartz in narrow, well-defined corridors have lobate boundaries against larger grains causing the previously described embayments (Fig. 8d,e).

Plagioclase composition varies with the width of corridors (Table 2). For small isolated pockets or narrow corridors (< 100 μm wide) plagioclase composition is albitic, reaching $An_{0–5}$ in the thinnest films (Figs 5a & 8e). Plagioclase in fine-grained bands also exhibits the same normal zoning as the large grains, with $An_{5–15}$ cores and more sodic ($An_{0–5}$), distinct, 5–10 μm thick rims when in contact with coarse grains (Fig. 8e). In wide corridors (> 100 μm wide), plagioclase has different compositions depending on its position (Figs 5d & 9a). Grains in the centre of the fine-grained region are more Ca rich ($An_{10–15}$) than those at the margins (Fig. 9a). Moreover, some plagioclase grains display multiple normal zoning, with diffuse boundaries between individual zones (Fig. 9a).

Plagioclase, K-feldspar and quartz grains in wider masses of fine-grained leucogranite form either well

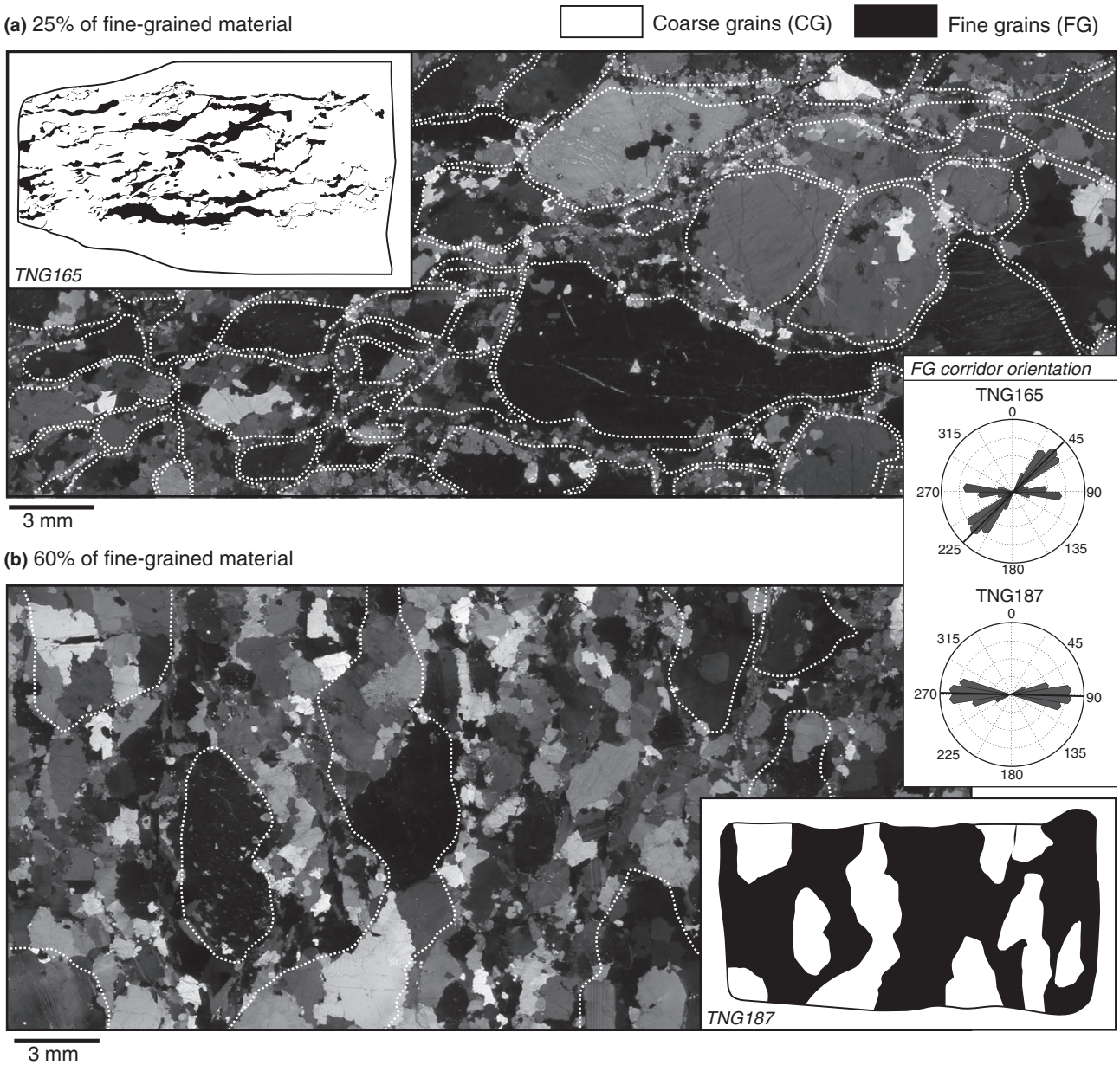

Fig. 6. Photomicrographs and sketches show different proportions of fine grains (FG) and coarse grains (CG) in leucosomes. Volume of fine-grained material in leucosomes varies from ~5–10 to ~80%. (a) Leucosome with ~25% of fine-grained material (sample TNG165). (b) Leucosome dominated (> 60%) by fine-grained material (sample TNG187). Insets depict the distribution of fine-grained (FG; black) and coarse-grained material (CG; white). The coarse crystals were distinguished using a combination of optical microscopy and BSE images, based on appearance – larger size, irregular shapes with embayed boundaries, optical continuity of disrupted grains, and composition. This process involves uncertainties related to image quality and difficulties in distinguishing crystal overgrowths. Distinction between fine and coarse grains becomes more difficult in samples with high proportion of fine-grained material, because of highly embayed to skeletal appearance of coarse grains, and coarser nature of fine-grained material in wider corridors. Estimated fine-grained modal proportions are considered to be a minimum value, with possible error of 0.5–5% (lower limit for samples with low fraction of fine grains; upper limit for samples with high fraction of fine grains). Coarse grains are outlined by white dashed line. Rose diagrams show preferred orientation of fine-grained corridors and bands in relation to foliation shown in insets. Notice two preferred corridor orientations at ~45° to each other in rose diagram and inset in (a).

developed, texturally equilibrated, foam-like textures with straight grain boundaries (Fig. 5d) or aggregates of grains with lobate boundaries (Fig. 5e,f). The fine grains are not visibly plastically deformed, and do not contain inclusions (Fig. 8).

Disequilibrium textures

The studied rocks typically have a number of textures commonly described in granitic and volcanic rocks and interpreted as disequilibrium textures (Fig. 10; e.g.

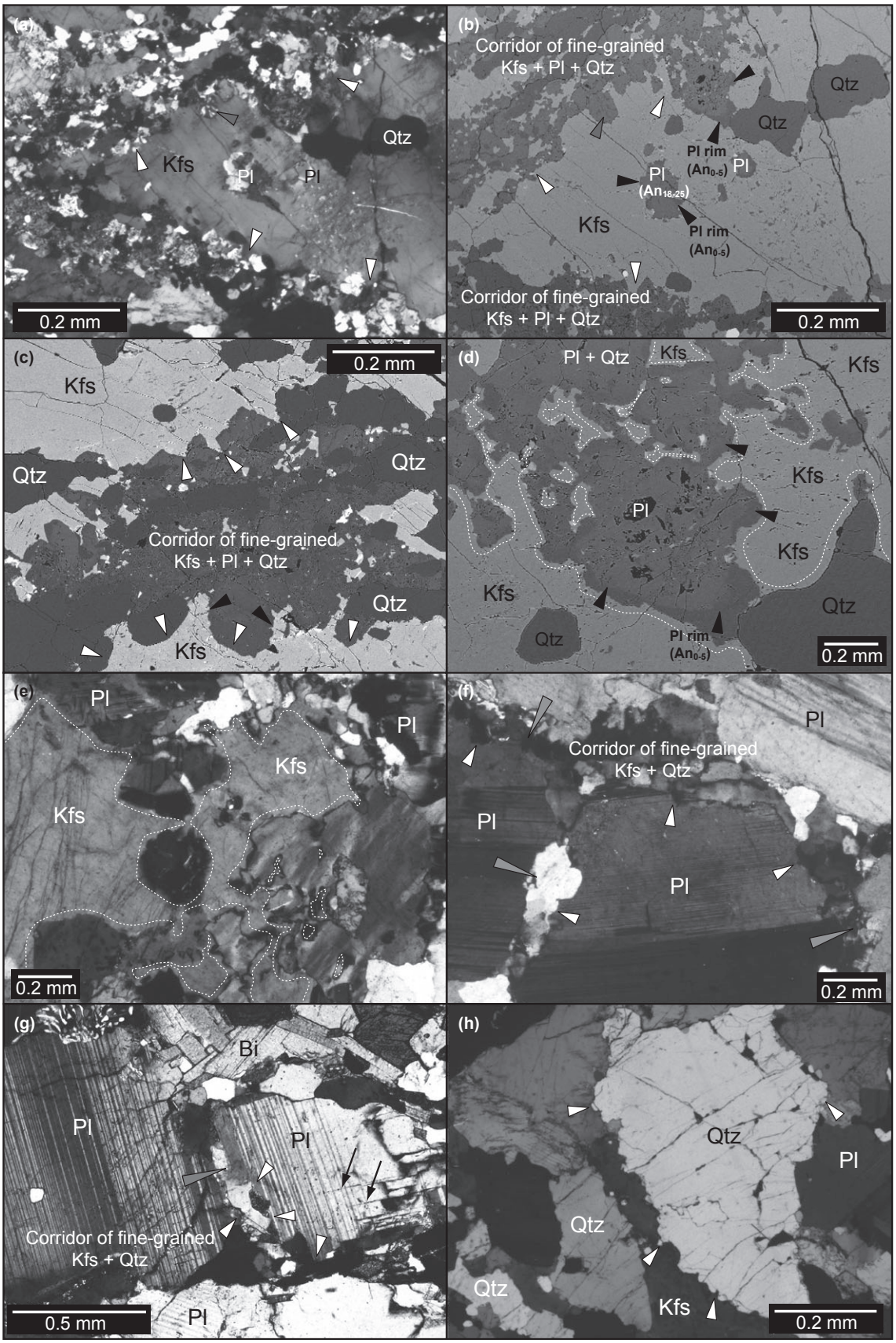

Hibbard, 1981; Flood & Vernon, 1988; Sawyer, 1999). (i) *Feldspar mantling*. Coarse, individual K-feldspar and plagioclase crystals are partially surrounded by a thin rim of plagioclase and K-feldspar crystals, respectively (10–50 μm; Fig. 10a,b). This texture is commonly interpreted as resulting from mixing of mafic and felsic magmas (e.g. Hibbard, 1981; Bussy, 1990). (ii) *Zoned inclusions*. Corroded, irregular plagioclase inclusion in coarse K-feldspar grains reveal zoning with oligoclase cores and more albitic rims (Fig. 10c,d, white arrows). Similarly, there are strongly corroded K-feldspar grains, ragged in shape, inside coarse K-feldspar. (iii) *High energy boundaries*. Coarse plagioclase and K-feldspar grains reveal embayed crystal shapes (Fig. 10e–h) indicating that they have been resorbed. (iv) *Compositional zoning of fine-grained feldspar* indicating chemical disequilibrium with coarse grains. Together, these features indicate that early formed crystals might have been out of equilibrium with the magma during later stages of crystallization.

Quartz cathodoluminescence

Both K-feldspar and plagioclase exhibit clear compositional zoning in BSE images reflecting different compositions, depending on their microstructural position (Figs 5b,d, 7b,d, 8e & 9a). Quartz does not reveal any internal textural features in optical or BSE images. However, under cathodoluminiscence (CL) quartz reveals textural complexity. CL images of quartz grains were studied in two representative samples: TNG165 and TNG131E (Fig. 6). Cathodoluminescence images were collected using a grating spectrometer equipped with a CCD detector fitted to the JEOL 8500F HyperProbe at CSIRO, Melbourne, Australia (MacRae *et al*., 2005). Polished thin sections were used, with the final lap being 20 nm colloidal silica. Prior to examination, the thin sections were coated with a 15 nm carbon film. Cathodoluminescence images of quartz grains were generated for a wavelength of 2.71 eV that is associated with Ti peak in quartz (Leeman *et al*., 2008; MacRae & Wilson, 2008).

Cathodoluminiscence images of coarse quartz grains either show homogenous luminescence intensities throughout the whole grain, lacking internal textures (sample TNG165), or reveal concentric zoning with dark/lower intensity luminescence core grading to a bright/higher intensity luminescence rims 15–300 μm wide (sample TNG131E, Fig. 9b). Fine-grained interstitial quartz grains show either the same concentric zoning as coarse quartz, with lower intensity core and bright/higher intensity luminescence rims (Fig. 9b), or homogenous luminescence. However, when homogeneous, the fine-grained quartz typically has higher luminescence intensity than homogeneous coarse quartz grains.

Quartz fabric

In order to document the possible differences in crystallographic preferred orientation (CPO) in quartz grains in the granitic rocks and in order to distinguish between magmatic and 'solid-state' fabric of coarse grains and fine-grained material, *c*-axis orientation of quartz was measured in the two representative samples (TNG165 & TNG131E; Fig. 11). In TNG165, ~25% of the sample is comprised of fine-grained material, in TNG131E, ~60% consists of fine-grained material (Fig. 6). Coarse quartz grains were evaluated separately from fine grains (Fig. 11) and *c*-axis orientations were determined using the Fabric Analyser G50 at Melbourne University, Australia (methods in Wilson *et al*., 2003, 2007). Based on a stack of photomicrographs, the axial distribution image (Sander, 1950) is generated with a spatial resolution of 5 and 3 μm pixel^{-1} and the *c*-axis orientations of each pixel can then be evaluated using the INVESTIGATOR software (Peternell *et al*., 2009). The *c*-axis orientations can be either collected automatically in a regular grid (e.g. for each pixel) or manually. Data were collected manually, which allows interactive indexing and enables choice of measured spot. We chose one spot for each area with different orientation (> 10° difference), i.e. per subgrain/grain, rather than evaluating every pixel (see Fig. 11a,b,d for data collection strategy). Thus, each individual grain/subgrain is represented by only one orientation measurement and we distinguished between quartz grains in fine-grained trails and coarse grains, and plotted them separately.

The measurements of coarse- and fine-grained quartz result in different *c*-axis patterns and fabric intensities. Coarse grains have strong CPO in comparison to the weak maxima defined by fine grains (Fig. 11c). Despite the lack of visible internal crystal

Fig. 7. Photomicrographs and backscattered electron (BSE) images showing typical features of coarse grains in leucosomes, and their relationships with fine-grained corridors. (a, b) Coarse, irregular K-feldspar grain with inclusions of plagioclase and quartz. It has embayed boundaries (white arrows) traced by fine-grained plagioclase and quartz. Myrmekitic patches are common along K-feldspar boundaries (gray arrow) and plagioclase inclusions are zoned with oligoclase core and albitic rim (black arrows); (c) highly irregular K-feldspar grain with well-developed embayments along the contact with fine-grained corridors (white arrows). In detail, embayments have irregular, high energy, corrugations (black arrows). K-feldspar grain is in optical continuity on both sides of the fine-grained corridor; (d, e) skeletal K-feldspar grains. Coarse K-feldspar grains in both images are all optically continuous. White dashed lines trace the relicts of a single, coarse K-feldspar. Black arrows point to compositional zoning in plagioclase evidenced in BSE images by darker rims. (f, g) Large irregular, slightly embayed (white arrows) twinned plagioclase grains commonly transected by corridors of fine-grained K-feldspar and quartz (gray arrows). Plagioclase grains are optically continuous and have numerous fractures (black arrows in g). (h) Large, irregular and weakly deformed quartz grains with lobate boundaries (white arrows) coated by fine-grained K-feldspar and plagioclase.

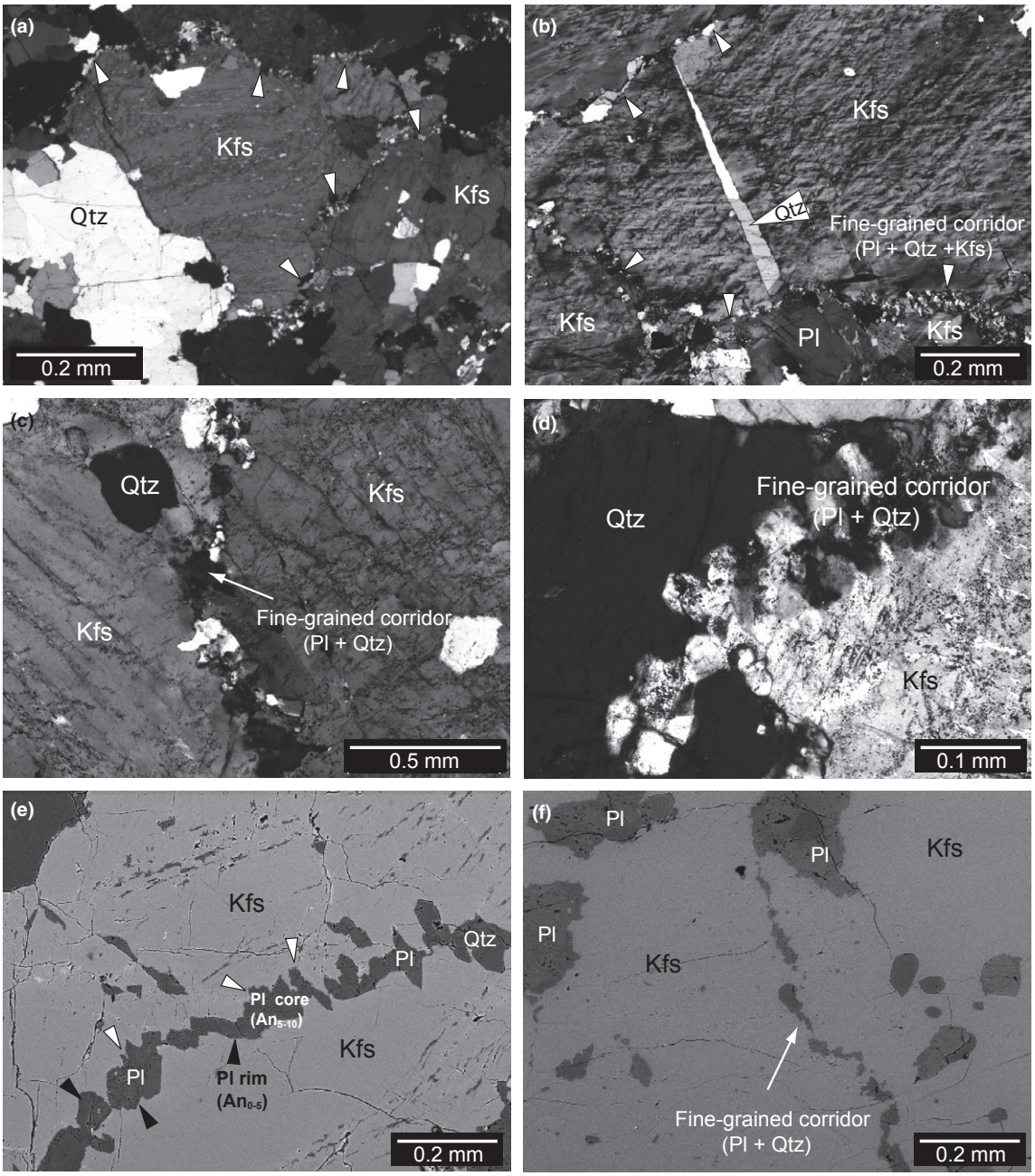

Fig. 8. Photomicrographs and backscattered electron (BSE) images showing main features of fine-grained material: (a) coarse K-feldspar grain with most of its faces coated by corridors of fine-grained material (white arrows); (b) coarse K-feldspar grain decorated with fine-grained material (white arrows) and cut by a planar crack filled with quartz, likely to be late- or post-magmatic; (c) detail of fine-grained corridor (plagioclase and quartz) cutting across a coarse K-feldspar grain; (d) detail of boundary traced by a narrow corridor of fine-grained material. Note the high-energy boundary of adjacent coarse grains of K-feldspar and quartz; (e, f) BSE images of narrow corridors of quartz and plagioclase in coarse K-feldspar. Plagioclase grains are zoned, with more albitic rims (black arrows). Note contrast in size and shape between grains in narrow corridors and the coarser, more euhedral pre-existing inclusions in K-feldspar on the right in (f). White arrows in (e) mark high energy, corrugated boundaries between fine grains and coarse K-feldspar.

deformation, coarse quartz grains reveal strong *c*-axis maxima indicating prism <a> slip-system in combination with minor rhomb <a+c> and basal <a> slip-systems (Fig. 11c). Activation of these slip-systems indicate deformation at lower to middle amphibolite facies conditions (< 650–680 °C; e.g. Schmid & Casey, 1986; Passchier & Trouw, 1996; Stipp *et al.*, 2002; Festa, 2009).

The *c*-axis orientation of fine-grained quartz shows an incomplete and slightly asymmetric girdle with an opening angle of > 90° and clear but weak maxima indicate activity of <c> prism slip-system (Fig. 11c),

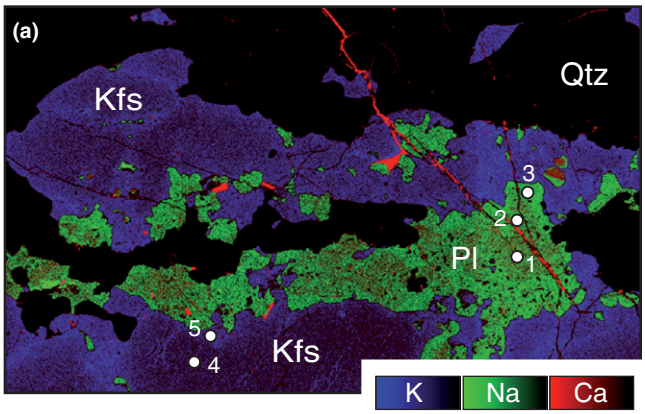

Mineral	Plagioclase			K-feldspar	
position	(1)	(2)	(3)	(4)	(5)
Wt % oxide					
SiO_2	65.35	66.76	67.95	65.34	65.23
Al_2O_3	22.03	21.18	19.43	18.66	18.52
CaO	3.16	1.78	3.05	0.05	0.00
Na_2O	9.76	10.59	11.89	2.98	0.93
K_2O	0.12	0.13	0.14	12.55	15.40
Total	100.42	100.44	99.58	99.58	100.07
Ab	**0.84**	**0.91**	**0.98**	**0.26**	**0.08**
An	**0.15**	**0.08**	**0.01**	**0.00**	**0.00**
Or	**0.01**	**0.01**	**0.01**	**0.73**	**0.92**

An = Ca/(Ca + Na + K); *Ab* = Na/(Ca + Na + K); *Or* = K/(Ca + Na + K)

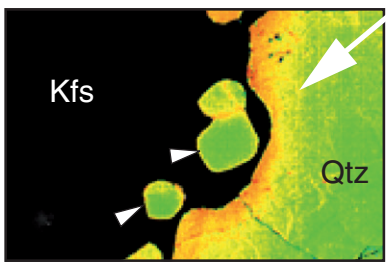

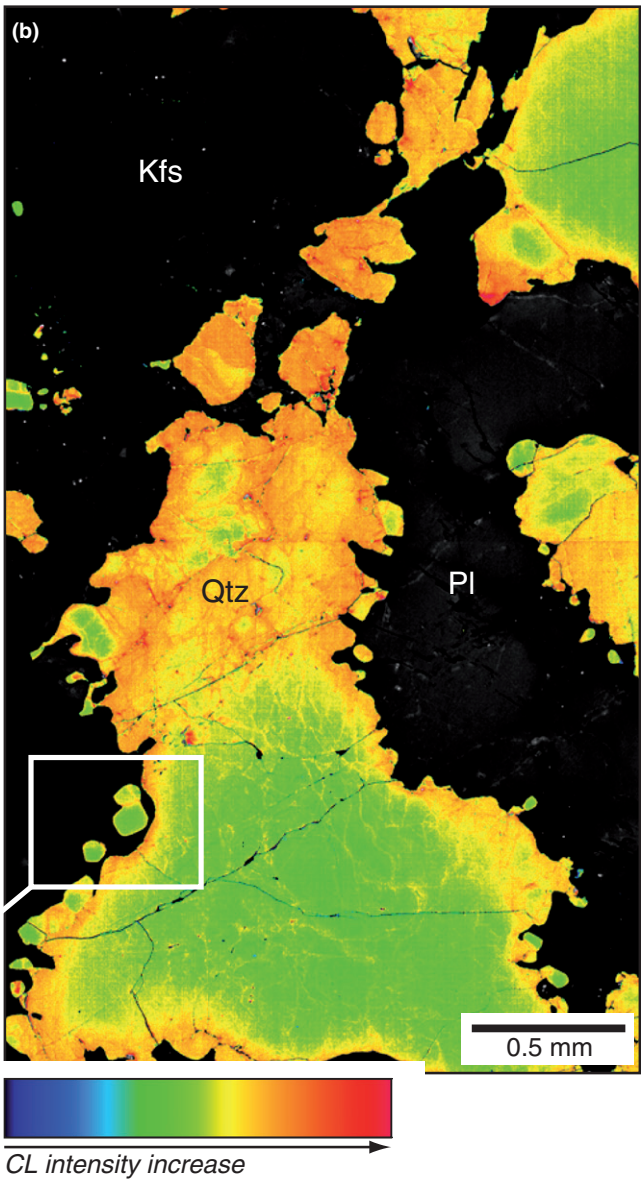

Fig. 9. Compositional zoning. (a) An elemental map showing zoning of both, plagioclase in fine-grained trails (in green) surrounding coarse K-feldspar grains (in blue; sample TNG165). K-feldspar zoning is characterized by more potassic rims (lighter blue). Plagioclase exhibits normal zoning with $An_{5–15}$ in core and $An_{0–5}$ in rims (lighter green) at contacts with K-feldspar. In this wide band of fine-grained granite, plagioclase has different composition in the centre compared to the border. Quartz is black. White numbered points represent analysed spots in feldspar: composition summarized in table. (b) Cathodoluminiscence image of quartz grains (sample TNG 131E). Both, coarse- and fine-grained (small inset) quartz grains reveal concentric zoning with dark/lower intensity luminescence core and bright/higher intensity luminescence rims. Notice irregular and embayed nature of contact against both the coarse K-feldspar and plagioclase grains.

indicative of high temperatures at granulite facies conditions (~750 °C at 5 kbar; Tullis *et al.*, 1973; Blumenfeld *et al.*, 1986; Mainprice *et al.*, 1986; Stipp *et al.*, 2002; Festa, 2009). This estimated temperature would be lowered by the presence of water (Tullis *et al.*, 1973; Passchier & Trouw, 1996; Mancktelow & Pennacchioni, 2004) that was documented in the studied area by Reichardt *et al.* (2010). The weak maxima defined by fine-grained quartz indicate direct crystallization from magma and contrast with the strong maxima of coarse grains indicating solid-state deformation overprint after crystallization (e.g. Schmid & Casey, 1986; Gleason *et al.*, 1993; Peternell *et al.*, 2010). Therefore the difference in fabric pattern and intensity between coarse and fine quartz grains reflect different temperatures associated with different processes.

Another important result is that the misorientation *c*-axis map reveals different quartz orientation at the rim compared to the core of the same grain, along

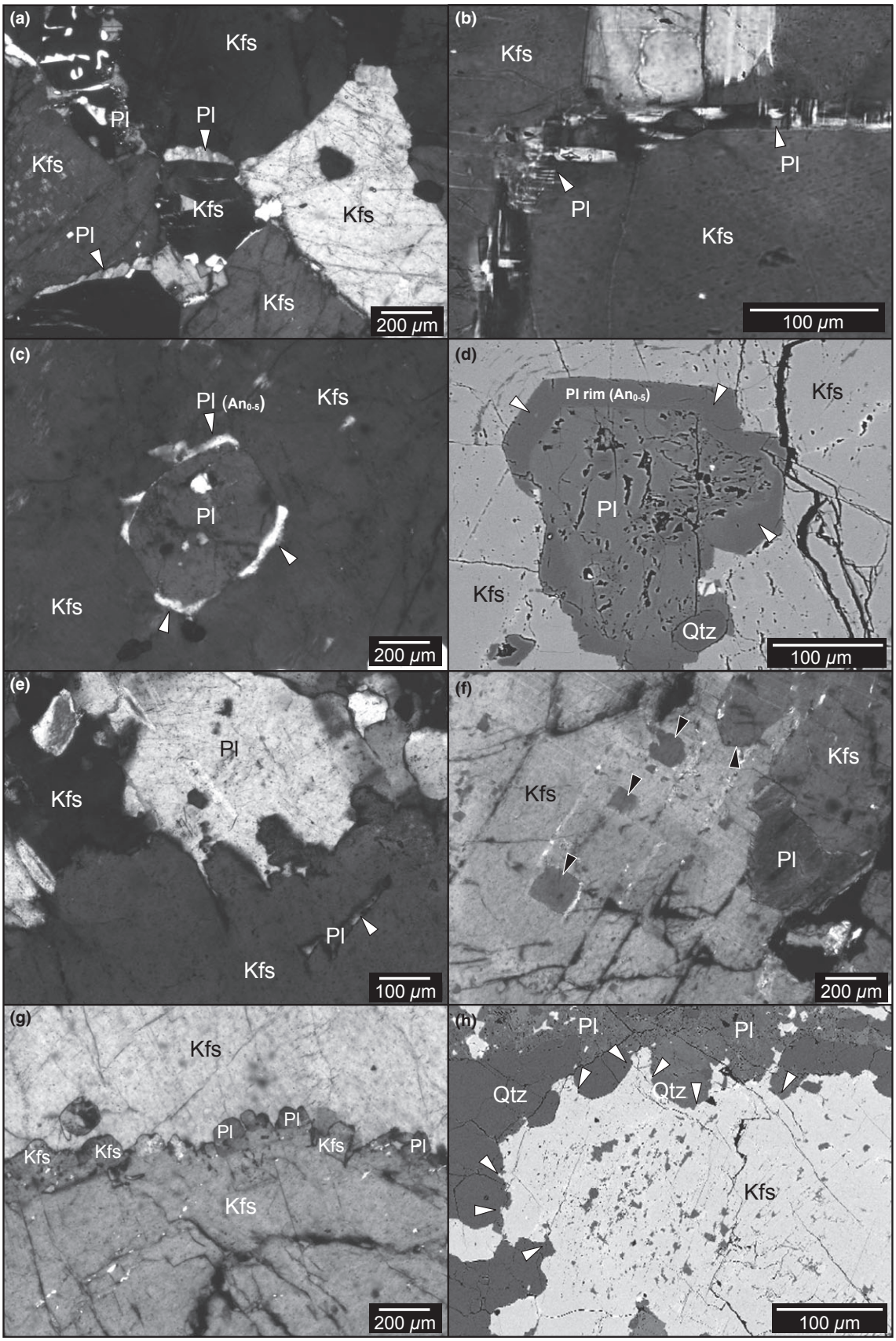

boundaries coated with fine-grained material. These rims are sharp, continuous and exclusively spatially related to the coated boundaries (Fig. 11a,b,d). This shows that quartz in fine-grained bands occurs either as new grains, growing with different orientation compared to pre-existing large grains (termed here 'overgrowth') or as individual, small new grains when not spatially close to large quartz grains (Fig. 11d).

In summary, granitic rocks from within the Karakoram Shear Zone are comprised of coarse-grained phases and fine-grained trails, corridors or bands of varying widths (Fig. 5). These either cross-cut coarse grains or follow grain boundaries. These boundaries are typically embayed, indicating possible reaction (Figs 7 & 10e–h). Mineral distribution in the fine-grained corridors are such that the corridors typically lack the mineral that comprises the coarse neighbouring grain (e.g. Fig. 8e–f), suggesting that this phase overgrew the coarse grain. This is supported by the compositionally different rims in coarse K-feldspar (Fig. 9a), more albitic rims in plagioclase and overgrowths on quartz grains demonstrated by CL images (Fig. 9b) and CPO images (Fig. 11).

DISCUSSION

Miocene leucogranitic rocks in the Pangong Range within the Karakoram Shear Zone have isotopic signatures intermediate between the two major anatectic source rocks exposed (Fig. 3). The microstructural, petrological and textural study presented suggests that several pulses of magma used the same pathways and interacted physically and chemically with crystalline material from earlier pulses. We suggest that early formed dykes provided a pathway exploited intermittently or continuously by new magma pulses and that the hybrid signature results from the interaction between new magma and previously crystallized magmatic rock through local equilibration. These features and hypothesis are discussed below.

Magma pathways on a microscale?

Magma distribution at outcrop scale is marked by the presence of leucocratic material as leucosomes, pockets, dykes and irregular bodies. These commonly form an interconnected magma transfer network (e.g. Sawyer, 2001; Vernon & Paterson, 2001; Marchildon & Brown, 2002; Weinberg & Mark, 2008). Exposures in the Pangong Range reveal an extensive interconnected network of leucosomes and dykes that commonly merge and diverge, rarely showing cross-cutting relationships (Fig. 2). This network has been interpreted as a magma transfer network linking the anatectic source and the Karakoram Batholith (Weinberg *et al*., 2009; Reichardt *et al*., 2010; Reichardt & Weinberg, in press).

In contrast, it is not always straightforward to infer former melt presence in rocks at microscale (e.g. Sawyer, 2001; Hasalová *et al*., 2008; Schulmann *et al*., 2009). Criteria for recognition of former melt have been summarized by many authors (for review see Sawyer, 1999, 2001) and include: (i) interstitial grains/films or cuspate pools between adjacent original grains, inferred to represent components of crystallized melt reflecting melt distribution (e.g. Jurewitz & Watson, 1984; Sawyer, 1999; Holness & Sawyer, 2008); (ii) normal zoning of plagioclase in contact with K-feldspar (e.g. Marchildon & Brown, 2001); and (iii) low Kfs–Kfs and Kfs–Kfs–Pl dihedral angles, typical for granitic melts (Laporte *et al*., 1997).

We have described and mapped the distribution and relationships between fine-grained granitic material and coarse-grained crystals in leucosomes and dykes (Figs 5, 6 & 8) including overgrowths of coarse grains (Figs 9 & 11), and multiple evidence for disequilibrium, such as high energy grain boundaries (embayments), and feldspar mantling (Fig. 10). These microstructures could be explained by three different possible mechanisms beyond our hypothesis that they represent melt paths through a solid granitic framework: (i) solid-state deformation (e.g. Nyman *et al*., 1992; Dunlap *et al*., 1997; Rosenberg & Riller, 2000; Stipp *et al*., 2002; Vernon *et al*., 2004; Oliot *et al*., 2010); (ii) late melt crystallization in a closed system (Hibbard, 1987; Flood & Vernon, 1988; Bouchez *et al*., 1992; Vernon, 2004); or (iii) sub-solidus hydrothermal alteration. We investigate these possibilities before returning to our main hypothesis.

Solid-state deformation

Peak metamorphic conditions during syn-kinematic Miocene anatexis (Fig. 12a) were estimated to have reached upper amphibolite conditions in the exposed migmatites of the Pangong Range (~700 °C; Rolland & Pêcher, 2001), i.e. sufficient to enable dynamic recrystallization to take place during subsequent cooling. Dynamic recrystallization, combining grain boundary migration and subgrain rotation, produces

Fig. 10. Photomicrographs and backscattered electron image of disequilibrium textures. (a, b) Rapakivi texture: Coarse K-feldspar grains mantled by thin rims of plagioclase (white arrows). (c, d) Zoned, corroded, irregular plagioclase inclusions in coarse K-feldspar grains, with oligoclase cores and albitic rims (white arrows). (e) Embayed plagioclase-K feldspar contact indicating destabilization of early crystallized coarse grains. Small plagioclase relict (white arrow) enclosed in surrounding K-feldspar is optically continuous with the coarse plagioclase and possibly was originally part of this grain. (f) Corroded contact between two coarse K-feldspar grains indicating destabilization of early formed grains. Note optically continuous remnants of one K-feldspar (black arrows) enclosed in the other K-feldspar. Remnants would have been originally part of the K-feldspar grain on the right. (g) Detail of high energy, corrugated boundary between two K-feldspar grains. Note fine plagioclase grains tracing this boundary. (h) Detail of high-energy embayed boundary (white arrows) between coarse K-feldspar grain and fine-grained quartz and plagioclase.

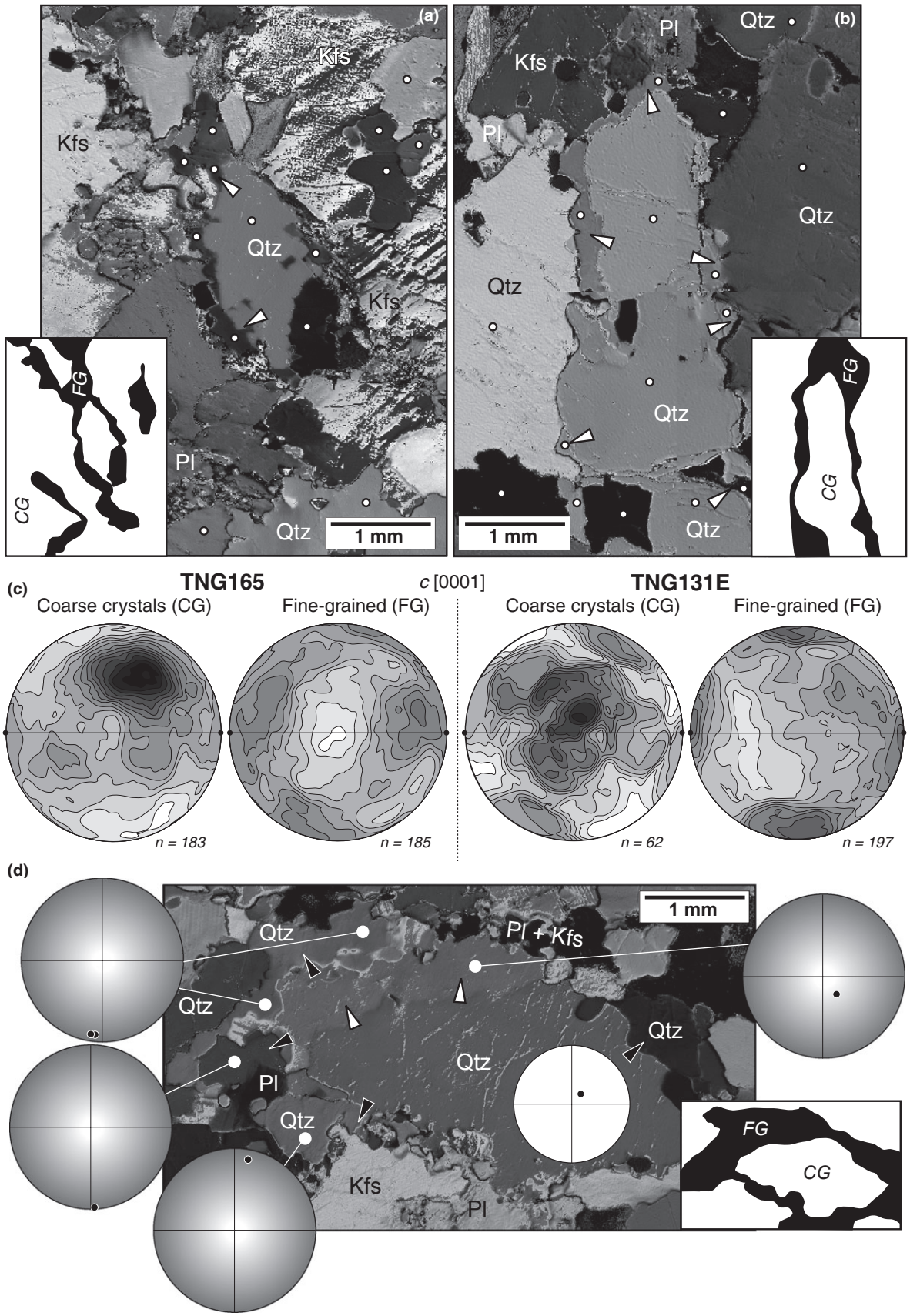

bimodal grain size distribution with large, irregular, lobate grains with sutured (grain boundary migration) or straight (subgrain rotation) boundaries, mantled by fine-grained recrystallized grains of uniform size (e.g. Vidal *et al*., 1980; Tullis & Yund, 1985; Stünitz, 1998; Stipp *et al*., 2002; Vernon *et al*., 2004). However, dynamic recrystallization causes reconstitution of grains without changes in chemical composition, producing fine, monomineralic aggregates compositionally similar to the porphyroclasts (e.g. Humphreys & Hatherly, 1996). Recrystallization involving changes in chemical composition (Stünitz, 1998) produces compositional differences between porphyroclasts and recrystallized grains. The differences arise from compositional adjustment to the equilibrium composition during recrystallization under given or changing *P–T* conditions. Given a simple heating history followed by cooling and insignificant post-metamorphic re-hydration of the system, recrystallized plagioclase grains will have different orthoclase and anorthite content than original porphyroclasts, but no new quartz and K-feldspar are expected to be formed (Stünitz, 1998; Franěk *et al*., 2011). Metamorphic recrystallization with chemical difference between porphyroclasts and recrystallized grains can also be forced by strain localization and influx of externally derived fluids (Oliot *et al*., 2010).

The expected nature of recrystallized material is incompatible with our observations that fine-grained corridors or bands consist of different proportions of all three minerals comprising a granitic rock (plagioclase, K-feldspar & quartz), or by two of these minerals with the third found as overgrowths on large grains (Figs 5, 7 & 12b,c) in the absence of evidence for alteration. Moreover, the fine-grained material is not uniform in grain size (Fig. 6) and lacks microstructures indicating extensive grain boundary migration, such as left-over grains, castellate, dragging, pinning, or window microstructures (Jessell, 1987; Stipp *et al*., 2002). Many of the lobate contacts are in between coarse grains of one mineral with fine-grained composite material. This is not a result of grain boundary migration related to dynamic recrystallization. Recrystallization can also be caused by cataclasis followed by fragment modification (Higgins, 1971; Means, 1989; Nyman *et al*., 1992; Stünitz, 1998; Vernon *et al*., 2004). This type of recrystallization is concentrated along internal deformation zones and forms small aggregates or patches of polygonal, angular grains of variable size and composition along grain boundaries. Vernon *et al*. (2004) pointed out that it might be difficult to distinguish microstructures formed by ductile recrystallization (dislocation creep/recovery) from the one originated by fracturing followed by growth and grain boundary migration. However, evidence for early, brittle deformation must be found.

The Miocene (20–15 Ma) anatectic event that generated leucosomes and granitic intrusions in the Pangong Range was followed by cooling with no evidence of a further heating event (Dunlap *et al*., 1998; McCarthy & Weinberg, 2010). Therefore, post-magmatic deformation is expected to record decreasing temperature, where ductile deformation is overprinted by brittle, such as the cataclastic deformation described by Rutter *et al*. (2007), lacking a later high temperature overprint. Our samples lack evidence for brittle deformation pre-dating high temperature deformation such as interstitial fine-grained material being originally fragments. These small grains are rounded to elongate with lobate boundaries (Fig. 8c–f) instead of angular, as expected for fragmentation (Nyman *et al*., 1992; Vernon *et al*., 2004). Similarly, wider bands of fine-grained material have low-energy polygonal to slightly lobate grains without evidence of fragmentation (Fig. 5c–f). Fine-grained plagioclase and K-feldspar also show clear compositional zoning (Figs 5d, 8e & 9a) whereas recrystallized grains are expected to be rather homogeneous, lacking zonation, except if alteration has affected the rock locally (Stünitz, 1998).

Quartz CPO results (Fig. 11c) show relatively strong maxima of coarse quartz grains indicating solid-state deformation overprint after crystallization. However, coarse grains of feldspar and quartz show little evidence of intracrystalline deformation (Figs 5 & 7). The most obvious is that large quartz grains display weak undulose extinction and locally forms subgrains (Fig. 5e) suggesting incipient recrystallization. The presence of myrmekite could also indicate solid-state deformation (Vernon, 1991), but could result directly from melt crystallization or reaction between solid and melt (Paterson *et al*., 1989).

Crystallographic preferred orientation results for fine-grained quartz indicate weak high temperature fabric. Poorly developed CPO in fine-grained quartz could reflect modification or obliteration of strong, deformation-related CPO patterns as a result of subsequent static recrystallization (e.g. Green, 1967;

Fig. 11. (a, b) Map of quartz *c*-axis orientations. Gray tones represent different *c*-axis orientation. Note fine-grained quartz overgrows coarse quartz grains, with different orientation (white arrows). White circles mark examples of measured *c*-axis orientation spots plotted in (c). Insets depict the distribution of fine-grained (FG; black) and coarse-grained material (CG; white). (c) Lower hemisphere, equal area stereonet projections of *c*-axis orientation of coarse and fine grains, contoured at interval of 0.3 times uniform distribution. Trace of foliation determined in the field is represented by horizontal black solid lines and *n* is the number of quartz analysis in each sample. *c*-axis orientation of coarse quartz defines maxima indicating activity of prism <a> slip-system in combination with minor rhomb <a+c> and basal <a> slip-systems. In contrast, *c*-axis orientation of fine-grained quartz defines weak maxima which indicate activity of <c> prism slip-system. (d) Detailed *c*-axis orientation image of coarse quartz (white stereonet) and its overgrowths (gray stereonet), as well as fine quartz grains in corridors (gray stereonet). Note different *c*-axis orientation for coarse quartz, its overgrowths (white arrows) and small single quartz grains (black arrows). Stereonet projections are similar to (c).

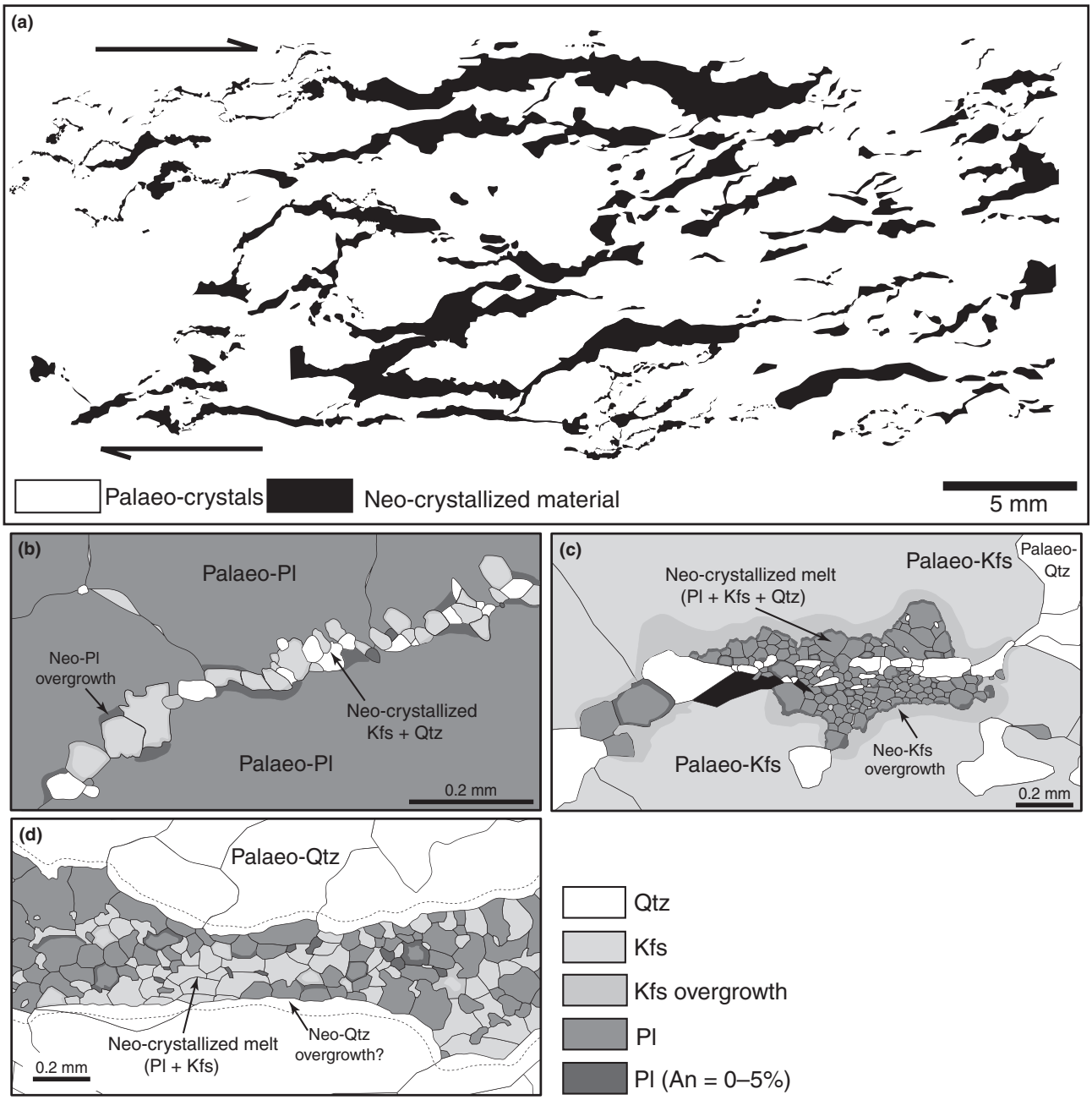

Fig. 12. (a) Thin section map showing the distribution of neo-crystallized material at micro-scale (sample TNG165). The neo-crystallized material forms an interlinked extensive network broadly defining an S-C fabric (syn-magmatic shearing). (b–d) Model of late melt granitic crystallization in channels. When new granitic melt invades a solid framework it crystallizes as Pl + Kfs + Qtz. It either crystallizes all three main granite, forming minerals along the corridor, or two of them with the third forming overgrowths on the surrounding pre-existing crystal (the 'complementary principle'). (b) Narrow corridor of fine-grained K-feldspar and quartz across coarse palaeo-plagioclase grains. Plagioclase melt component crystallizes as overgrowths on pre-existing plagioclase. (c) Pool of neo-crystallized plagioclase (with albitic rims) and quartz between two palaeo K-feldspar grains. K-feldspar melt component crystallizes as overgrowths on pre-existing K-feldspar. (d) Wide path of neo-crystallized plagioclase and K-feldspar across palaeo-quartz. Quartz melt component may have formed overgrowth on surrounding quartz.

Stöckhert & Duyster, 1999; Heilbronner & Tullis, 2002). Although this suggestion is supported by some experimental work (Ree & Park, 1997; Heilbronner & Tullis, 2002), recent observations on naturally occurring quartz CPO patterns show that effects of static recrystallization are minor and, even after extensive static recrystallization, quartz CPO originally present remain intact (Otani & Wallis, 2006). Static recrystallization would also produce well-equilibrated polygonal mosaic of grains (e.g. Passchier & Trouw, 1996),

which we observe only locally and only in larger aggregates (Fig. 5c,d). Most significantly, it would destroy the high-energy boundaries documented (Fig. 10e–h). Moreover, sample TNG131E, with ~60 vol.% of fine-grained material, has slightly stronger maxima than sample TNG165, with ~25 vol.% of fine-grained material (Fig. 11c). If the weak quartz fabric reflects later overprint by static recrystallization, sample TNG131E would have been more strongly overprinted and therefore should have a weaker fabric, contrary to the observed.

We therefore infer that weak quartz CPO of fine-grained bands reflects crystallization from melt, without the involvement of solid-state deformation, at higher temperatures than the CPO of coarse grains, which indicate a weak amphibolite facies sub-solidus deformation. Thus, our granitic rocks have two distinct grain generations: (i) an older generation comprising coarse crystals that record high temperature solid-state deformation under decreasing temperature conditions; and (ii) a younger generation of fine-grained crystals that lack intracrystalline deformation features, and define weak CPO, indicating crystallization from a later melt.

Late melt crystallization in a closed system

Continuous crystallization of granitic magma commonly results in bimodal grain size distribution, with large phenocrysts isolated in a mass of fine-grained crystals (e.g. Hibbard, 1965, 1987; Miller & Paterson, 1994; Vernon, 1999, 2004). Coarse grains or coarse grain aggregates in the Pangong Range leucogranitic rocks lack typical features of porphyritic magmatic rocks, such as oscillatory zoning, euhedral shapes, simple twinning, or zonally arranged euhedral inclusions (e.g. Vernon, 1990). Instead, coarse grains comprise all three felsic phases (Figs 7 & 12b–d), have strongly corroded shapes (Figs 7a–e & 10e–h) and most of their grain boundaries are coated by corridors of fine-grained granitic material (e.g. Figs 5a,b & 8).

Unlike typical porphyritic texture where phenocrysts are surrounded by a finer-grained matrix, in the Pangong Range leucogranites, fine-grained granitic tracks form a continuous or semi-continuous extensive network branching around and cross-cutting the large grains (Fig. 12a). In extreme cases, these trails become sufficiently wide and corrode pre-existing coarse grains that then become isolated, optically continuous islands in thin section (Figs 6 & 7). Embayments or corroded shapes in contacts with fine-grained granitic material indicate that coarse grains were part resorbed and imply disequilibrium between grain and melt. Thus, we infer that the texture is not a result of closed crystallization of a magma giving rise to a porphyritic texture.

Deformation during magma crystallization gives rise to characteristic features that indicate the presence of interstitial melt. Criteria for recognition of sub-magmatic deformation were summarized by many authors (for review see Blenkinsop, 2000; Vernon, 2004) and include: fractures filled with melt (e.g. Hibbard, 1987; Bouchez *et al.*, 1992; de Saint Blanquat & Tikoff, 1997; Vernon, 2000; Vernon *et al.*, 2004), presence of late crystallized material in strain shadows (Gapais & Barbarin, 1986; Bouchez *et al.*, 1992; Vernon, 2000) and contact melting reflecting a solution process in deforming melt-present systems (Park & Means, 1996; Vernon, 2000; Vernon *et al.*, 2004). Pangong Range leucogranites have features indicative of crystallization during deformation. The most obvious are sharp fractures in large crystals intruded by fine-grained granitic material (e.g. Fig. 8b). These are common, but differ from the narrow, tortuous corridors described above which can cross-cut several large grains (Figs 5 & 8a,c,d).

Sub-solidus hydrothermal fluid alteration

Late stage magmatic hydrous fluids are expected to circulate along grain boundaries and fractures, causing local dissolution and precipitation, modifying the original magmatic texture. In this case, fine-grained feldspar and quartz could be deposited and large crystals corroded. However, hydrothermal alteration is expected to be accompanied by secondary minerals such as chlorite, white mica, epidote or alteration of existing minerals, such as feldspar sericitization. We would also expect hydrothermal veins, or increased concentration of fluid inclusions in particular zones. None of these features has been documented.

In summary, the textures described are unlikely to be the result of solid-state deformation, or to represent a porphyritic texture resulting from closed system syn-kinematic crystallization, or hydrothermal alteration. We now turn to our main hypothesis that the features represent melt pathways in a previously formed solid granitic framework.

Open-system magma pathways

Here the possibility that the textures result from an open system, where different magma batches use the same pathways is discussed. Late batches exploit microfractures in between and through crystals formed from earlier batches, giving rise to an interconnected network (Fig. 12a). The large, framework-forming grains are referred to as palaeo-crystals, in contrast to neo-crystals which refer to the newly crystallized, finer material forming the network (Fig. 6).

We first focus on evidence that the finer-grained corridors represent interstitial, late crystallized melt, and then expand this interpretation to include the nature of these pathways, the volume of melt involved, the mechanism for re-opening of these channels (why should new batches of melt reuse old channels?), and the possibility of multiple repetitions of this process. Finally, we discuss the importance of this process for

isotopic mixing and its implications for calculations of melt fluxes through leucosomes and dykes.

Evidence for open-system leucogranite formation

When a new magma batch flushes through a granitic rock or a mush of crystals and interstitial melt, differences between the inflowing magma and resident solid phases result in textural and chemical disequilibrium features. This is manifested along the interconnected networks formed by neo-crystallized granite (Figs 7–10).

Textural disequilibrium. Evidence for disequilibrium includes palaeo-grains with irregular, high energy, slightly to strongly corroded shapes at boundaries coated by newly crystallized material (Figs 7 & 10e–h), as well as feldspar mantling (Fig. 10a,b). Disequilibrium is also indicated by bulbous myrmekite and highly irregular lobate grains that overgrow partially resorbed, corroded feldspar grains, similar to microstructures typical of minerals reacting with melt (Mehnert *et al.*, 1973; Büsch *et al.*, 1974; McLellan, 1983).

Chemical disequilibrium. Intrusion and crystallization of a late granitic melt to explain the narrow fine-grained bands is supported also by compositional zoning of all major felsic phases (Fig. 9). Simple granitic melts close to the eutectic composition are comprised almost entirely of combinations of Qtz + Kfs + Pl. If a new melt batch invades a solid framework of feldspar and quartz, it either crystallizes all three felsic phases, or two felsic phases, forming the bulk of the dykelet, whereas the third phase either crystallizes as overgrowths on the neighbouring palaeo-crystal or elsewhere along the dykelet ('the complementary principle' defined in Fig. 12 see also Fig. 13). All three felsic minerals in different places of the thin sections reveal these overgrowths (Figs 12c,d & 13). Quartz overgrowths were documented by CL, and different CPO of early formed coarse quartz and its rims (Figs 9b & 11). Both, plagioclase and K-feldspar palaeo-grains have compositional zoning at boundaries lined with neo-crystallized material: oligoclase is rimmed by albite, and orthoclase is rimmed by more potassic rims (Fig. 9a; Table 2).

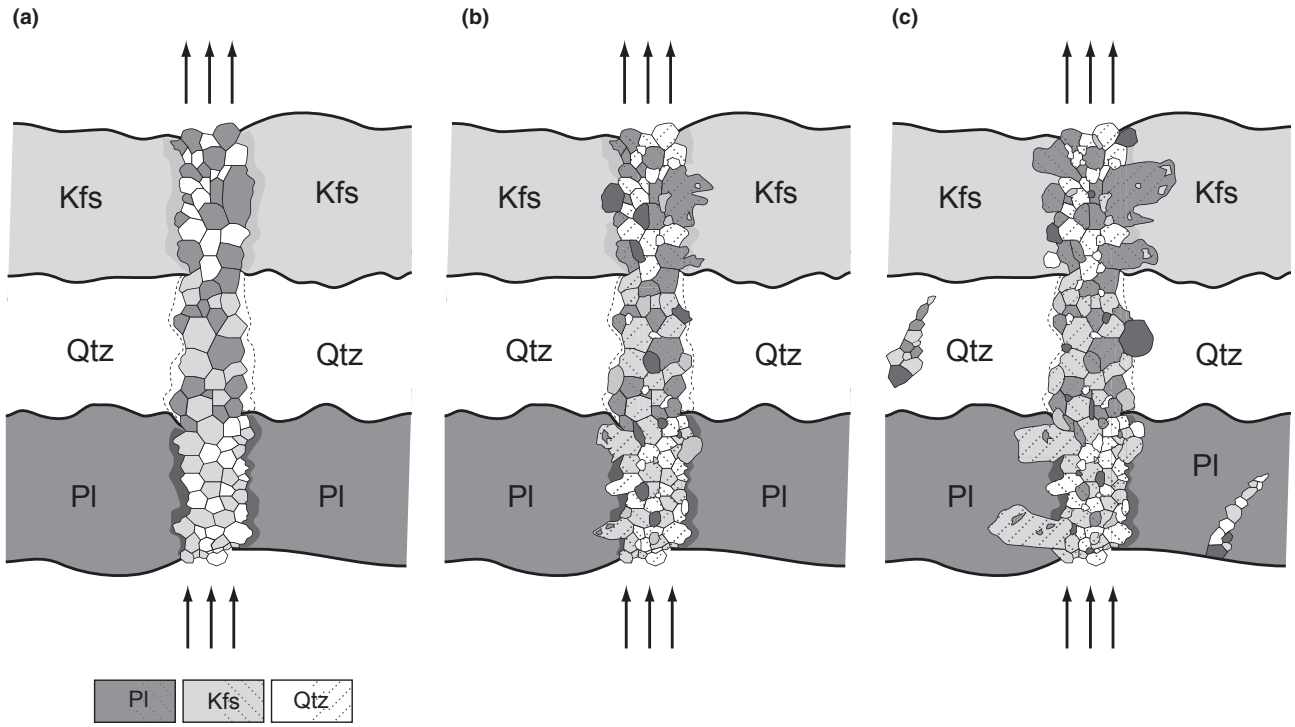

Fig. 13. Schematic model of crystallization along microscopic melt paths through pre-existing solids and temporal evolution of these channels, illustrating the possibility of multiple melt injections. Grain size in intrusive corridor depends on its width. Sequence from (a) to (c) reflects incremental growth of the microscopic channels in time. (a) Granitic melt crystallizes and equilibrates with previously crystallized magmatic rock, forming a narrow path of neo-crystallized Kfs + Pl + Qtz. (b) Another melt batch uses previously formed narrow path. This new melt batch equilibrates texturally and chemically with solid palaeo-crystals forming chemical zonation in feldspar and corroded shapes of palaeo-crystals. Note two of the main granite forming minerals crystallize along the corridor and the third overgrows the surrounding pre-existing crystal (the 'complementary principle'). (c) Multiple re-usage of pathway. Corroded shapes of palaeo-crystals become more pronounced. Hatched and non-hatched grains reflect compositionally different grains corresponding to different melt batches. Non-hatched grains in (a) equilibrates with a new magma batch and form different grains shown as hatched grains in (b). This process is again repeated in (c).

The measured CL intensity in quartz has been previously reported to be proportional to Ti concentration (Rusk *et al*., 2006; Spear & Wark, 2009), which further correlates with temperatures at the same pressure, with higher Ti concentrations reflecting higher temperatures (Wark & Spear, 2005; Wark & Watson, 2006; Thomas *et al*., 2010). This assumes constant Ti concentration in the system for a fixed activation, a_{TiO_2}, value for the whole magmatic history (e.g. Wark *et al*., 2007; Wiebe *et al*., 2007). However, melt saturation in Ti may vary (especially in open system) and therefore measured CL intensity may reflect either different temperature or different a_{TiO_2} in the melt.

Quartz palaeo-crystals have distinct rims (15–300 μm wide) with higher Ti concentrations at boundaries lined with neo-crystallized material (Fig. 9b). Thus, quartz overgrowths indicate that the new magma pulse had higher crystallization temperatures or higher Ti activities than the original. An alternative interpretation is that the bright rims result from diffusive exchange with the neo-crystallized material (Spear & Wark, 2009), but Ti diffusion in quartz at ~700 °C and 5 kbar is expected to be limited and only produce thin Ti-rich rims (Cherniak *et al*., 2007). However, we cannot rule out that some diffusion and later solid state recrystallization might have affected the final quartz CL zoning pattern (e.g. Spear & Wark, 2009). Single quartz neo-crystals in fine-grained trails reveal either the same zoning as palaeo-quartz grains (inset in Fig. 9b) or are homogeneous but with higher Ti concentrations, indicating higher crystallization temperatures or higher Ti activities in the late melt, than for the original palaeo-crystals. This supports the idea of a later and different melt crystallizing either as small new grains or as overgrowths on early crystallized grains (Fig. 12b–d).

This interpretation is further supported by *c*-axis orientation maps of quartz palaeo-grains, which display different orientations at the rim and in the core of the same grain along boundaries coated with fine-grained neo-crystals (Fig. 11a,b,d). In cataclasites or proto-mylonites, it is common for narrow rims of an optically strained grain to surround a strain-free core. However, in the rocks described here the rims are sharp, continuous and exclusively spatially related to the coated boundaries (Fig. 11a,b,d). Difference in *c*-axis orientation related to solid-state deformation would not be limited to boundaries coated by fine-grained material. Additionally, these rims reveal weak CPO (they are included in fine-grained quartz measurements in Fig. 11c) in contrast to quartz cores that have stronger CPO (included in coarse quartz in Fig. 11c). We interpret this difference in CPO pattern and intensity as indicative of fine-grained quartz growth on coarse quartz grains (Fig. 11d), not solid-state deformation of coarse grains.

It is tempting to compare the variation of plagioclase composition with width of corridors and pockets (more albitic in the thinnest films) with the findings of Holness & Sawyer (2008) who showed that plagioclase crystallized initially in the widest regions as Na-poor plagioclase, and then proceeded to crystallize in narrow regions as Na-rich plagioclase. However, here it was found that Na-rich plagioclase formed also in pores wider than the 20 μm across, in contrast to the findings of Holness & Sawyer (2008). A further difference is that plagioclase in our samples overgrew pre-existing plagioclase rather than filling entire pores. In larger pools or wider corridors, plagioclase reveals a variety of compositions depending on its position, being more calcic in the centre (Fig. 9a). Some neo-crystallized plagioclase displays multiple normal zoning, with diffuse boundaries between individual zones reflecting either continuous or multiple equilibration events. The compositional zoning of fine-grained material in general (Figs 8e & 9a) could result from two different processes. One is that melts of different composition have been added in multiple pulses so that the composition of the system changes with time. In this case, zoning is a result of equilibration between new magma and existing solids (open-system) and rims reflect new crystal growth. The other alternative is that of a closed system, with melt composition evolving as crystallization progresses. In this case, zoning results from interaction between early crystallized grains and the evolved, fractionated melt, and rims reflect a more evolved composition than the cores. Both scenarios are possible and we are unable to differentiate between them based on zonation alone.

Nature of magma pathways: continuous or intermittent influxes?

Disequilibrium textures could be related not only to initial differences in composition between intruding magma and resident crystals, but also to changes in *P–T* conditions over time, or to the evolving nature of the intruding magma as it equilibrates locally with different minerals comprising channel walls (Fig. 13). The main difference between samples is the amount of newly crystallized material (Fig. 6). The larger the proportion of neo-crystals, the less the original texture is preserved and the wider the pathways are (Fig. 6).

Mapping of the fine-grained corridors reveal that they form long interconnected networks over distances corresponding to several large, palaeo-crystals, sometimes crossing entire thin sections (Fig. 12a). Fine-grained corridors in some samples follow two distinct orientations (Fig. 6), reflecting the S-C fabric resulting from shearing. Based on the multiple lines of evidence that magmatism was contemporaneous with deformation (e.g. CPO results, and evidence for syn-magmatic fracturing of crystals) we interpret that the interlinked network intruded along an actively shearing rock mass.

We are currently unable to resolve whether magma flow through the network was continuous or

intermittent, or to recognize whether more than one new pulse of magma intruded a pre-existing solid framework. It is possible that the features documented could result from a number of new batches passing through the rocks as suggested for example by CL zoning of both coarse palaeo-quartz grains and fine, neo-crystallized quartz grains (inset in Fig. 9b).

Volume of melt involved

Estimates of the percentage of neo-crystallized material in pre-existing solid leucogranites are shown in Figs 6 and 12a. These were reconstructed combining optical and BSE images which allows recognition of overgrowth of albite around older plagioclase grains, but does not allow recognition of either quartz or K-feldspar overgrowths. Therefore, estimates of the volume crystallized from a later batch represent a minimum value. The question is then how much melt there may have been at any point in time through this network, or even whether it represents one new intrusion or many. Our impression is that the process and the final product are analogous to the growth of quartz veins in hydrothermal systems in that they represent a time integrated result of crystallization that does reflect neither the volume of liquid at any point in time, nor a direct measure of the total volume that passed through the network. Slagstad *et al*. (2005) argued that in their rocks melt must have migrated pervasively, several kilometres through hot rocks to produce the stromatic migmatite with up to 50% of leucosomes. They also argued that this must have been accomplished progressively and that the volume of leucosome is a result of cumulative addition of material over time, otherwise the stromatic migmatite would have lost continuity and move *en masse*. Similarly, some samples of Karakoram leucogranite investigated here have up to 80% of neo-crystallized material but did not lose continuity, suggesting that neo-crystals accumulated gradually. This is also supported by relatively strong CPO of quartz palaeo-crystals in samples with high percentage of neo-crystallized material (e.g. sample TNG131E in Fig. 11c). A strong CPO of quartz palaeo-crystals suggests deformation by dislocation creep in quartz which requires a solid-framework during deformation (e.g. Rosenberg & Handy, 2005).

Mechanisms

Magma migration within the Karakoram Shear Zone involves both creation of new paths as well as re-usage of previously formed paths, the main focus here. We envisage two possible mechanisms to explain path re-usage: (i) higher values of bulk modulus or lower yield strength of magmatic rocks compared to country rocks could favour preferential crack propagation in early crystallized leucogranites; (ii) if there remains an interconnected network of interstitial melt within a solidifying network of dykes linked to a large magma source, pressure increase in the source is transmitted across the entire network, causing stress amplification at narrow, melt-filled crack tips, and crack propagation into solid rock and magma migration.

Implications

Isotope mixing

Anatectic products within the Karakoram Shear Zone in the Pangong Range, including leucosomes in stromatic migmatites, have hybrid isotopic signatures that do not correspond to that of the immediate source rock (Reichardt *et al*., 2010). This implies that stromata, commonly interpreted as being nearly *in situ*, were in fact part of a magma transport channel network connecting magmas derived from different sources. Our textural investigation indicates that the likely cause of hybridization is the continuous or intermittent use of magma channelways, tapping magmas from different sources and allowing for local re-equilibration between melt and solids (Fig. 13). This process is distinct from the more generally assumed process of magma mixing used to explain magma hybridization.

The chemical composition of the magma flushing through the magma transfer network and out of it will vary and evolve in time, depending on starting composition and specific path through the network. Similarly the composition of the residual solid in stromata and dykes is the integral of each incremental growth, and sample the variety of magmas that flowed through the system. The evolution of a particular melt volume as it travels through the network is unpredictable. The melt does not evolve along a simple fractionation trend, but is continuously in the process of re-equilibrating with the immediate surroundings at grain scale. It is this process that leads to the combined textural, microstructural and chemical patterns documented here. The chemical evolution thus depends on specific paths and history within the network. However, on average this process will tend towards homogenization of any initial isotopic heterogeneities (Reichardt *et al*., 2010), while allowing also for magma fractionation as a result of crystallization and physical filtering of crystals.

Once an extensive channel network of this kind is established, major changes in the nature of the inflowing magma are attenuated by equilibration with resident material, and recorded only by gradual changes of the outflowing magma. Thus, magmas flowing out of this network to form a pluton are likely to evolve gradually reflecting a combination of changes in the source buffered by homogenization and fractionation along the way.

Dyke width

If leucosomes and dykes grow incrementally by means of cryptic microscopic channels (Fig. 13), then their

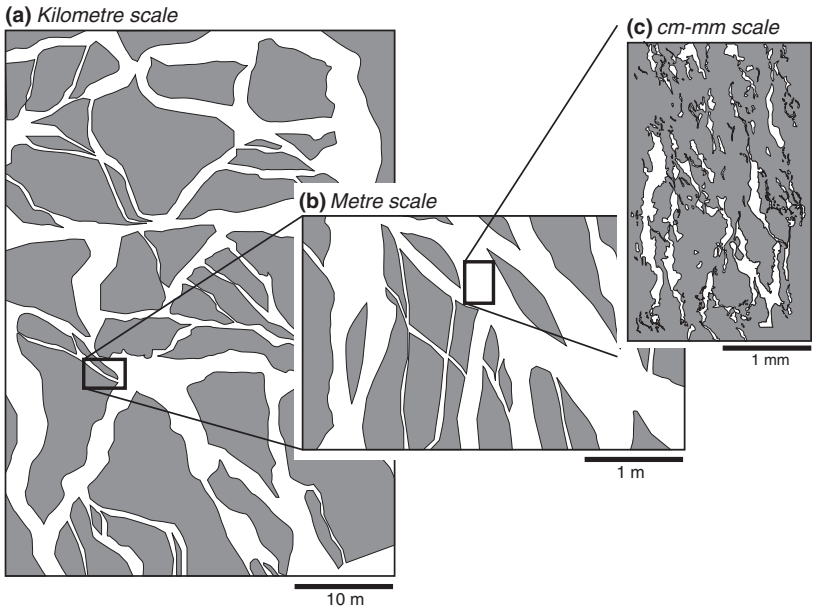

Fig. 14. Multiple scale nature of the interconnected magma drainage network: (a) Anastomozing leucogranite dykes, merging and diverging without truncations at 100 m to km scale. (b) Interlinked dykes at outcrop scale. (c) Microscopic channelways at thin section scale.

final widths and the integrated volume of magmatic rocks in any particular outcrop cannot be used directly to infer the geometry or nature of the network at the time of magmatism. For example, the distribution of leucosomes in migmatites may not record the volume of magma produced *in situ*, or dyke width may not represent its active width at the time of magma flow, and therefore cannot be used to estimate directly magma flux rates through the system. Thus, preserved dyke widths may indicate maximum rather than minimum widths as suggested by Marchildon & Brown (2003).

Link between small and large scale network

The dyke swarm in the Karakoram Shear Zone has only relatively rare cross-cutting relationships and typically anastomoze, merge and diverge seamlessly (Figs 2 & 14a; Weinberg & Regenauer-Lieb, 2010; Reichardt & Weinberg, in press). Some outcrops show a large volume of interlinked leucogranite dykes (Fig. 2). If these were connected and filled with magma simultaneously, the whole rock would have flowed *en masse*. The multi-channel, multi-usage process of magma migration at microscopic scale envisaged here could also explain the origin of these large interconnected systems. The large version may essentially be a magnified version of the small scale features (Fig. 14), whereby channelways developed at multiple scales, forming networks of dykes which expand with time, both in extent by new batches intruding fresh rock, and in width by new batches intruding older leucogranites. If each dyke in a network was formed by the gradual addition of crystalline material through multiple reactivation, this would tend to erase any cross-cutting relationships that may have developed during the early part of their growth.

CONCLUSIONS

In the Pangong Range, leucogranite dykes and leucosomes form an extensive interconnected network that links the Karakoram Batholith with its anatectic source. The network is characterized by continuous and interconnected dykes. A number of microscopic features have been described which suggest the presence of a similarly extensive magma network at microscopic scale within dykes and leucosomes. We argue that this network represents magma pathways that have exploited intermittently or continuously pre-existing magma channelways partly or entirely crystallized into granitic rocks. When a new magma batch flushes through a granitic rock, differences between the inflowing magma and solid phases result in textural and chemical disequilibrium features as documented here. New magma influx opens narrow channels and migrates pervasively. The final large scale network is a result of the integrated crystallization of each magma batch, and expands with time in extent and width, so that leucosomes and dykes reflect neither the volume of melt at any point in time, nor the total volume that passed through the system. Microscopic re-equilibration through re-usage of channels by different batches ultimately caused hybridization as recorded by a mixed isotopic signature in leucosomes and dykes in the magma transfer network in the Pangong Range, as well as in the Karakoram Batholith.

ACKNOWLEDGEMENTS

We acknowledge M. Peternell and G. Hutchinson (University of Melbourne) for assistance with the Fabric Analyser measurements and for assistance with the microprobe respectively. R. Vernon, E. Sawyer and

M. Holness are thanked for discussions. We also thank G. Zellmer and an anonymous reviewer for their constructive reviews.

REFERENCES

Beard, J.S., Ragland, P.C. & Crawford, M.L., 2005. Reactive bulk assimilation: a model for crust-mantle mixing in silicic magmas. *Geology*, **33,** 681–684.

Berger, A., Burri, T., Alt-Epping, P. & Engi, M., 2008. Tectonically controlled fluid flow and water-assisted melting in the middle crust: an example from the Central Alps. *Lithos*, **102,** 598–615.

Blenkinsop, T.G., 2000. *Deformation Microstructures and Mechanisms in Minerals and Rocks*. Kluwer, Dordrecht.

Blumenfeld, P., Mainprice, D. & Bouchez, J.L., 1986. *C*-slip in quartz from subsolidus deformed granite. *Tectonophysics*, **127,** 97–115.

Bouchez, J.L., Delas, C., Gleizes, G., Nédelec, A. & Cuney, M., 1992. Submagmatic microfractures in granites. *Geology*, **20,** 35–38.

Büsch, W., Schneider, G. & Mehnert, K.R., 1974. Initial melting at grain boundaries. Part II: Melting in rocks of granodioritic, quartz dioritic and tonalitic composition. *Neues Jahrbuch Für Mineralogie Monatshefte*, **8,** 345–370.

Bussy, F., 1990. The rapakivi texture of feldspars in a plutonic mixing environment: a dissolution-recrystallization process? *Geological Journal*, **25,** 319–324.

Cherniak, D.J., Watson, E.B. & Wark, D.A., 2007. Ti diffusion in quartz. *Chemical Geology*, **236,** 65–74.

Clarke, D.B., Henry, A.S. & White, M.A., 1998. Exploding xenoliths and the absence of 'elephants graveyards' in granite batholiths. *Journal of Structural Geology*, **20,** 1325–1343.

Crawford, M.B. & Searle, M.P., 1992. Field relationships and geochemistry of precollisional (India–Asia) granitoid magmatism in the central Karakoram, northern Pakistan. *Tectonophysics*, **206,** 171–192.

Crawford, M.B. & Windley, B.F., 1990. Leucogranites of the Himalaya/Karakoram: implications for magmatic evolution within collisional belts and the study of collision related leucogranite petrogenesis. *Journal of Volcanology and Geothermal Research*, **44,** 1–19.

DePaolo, D.J., Perry, F.V. & Baldridge, W.S., 1992. Crustal vs. mantle sources of granitic magmas: a two parameter model based on Nd isotopic studies. *Royal Society of Edinburgh Transactions, Earth Sciences*, **83,** 439–446.

Dunlap, W.J., Hirth, G. & Teyssier, C., 1997. Thermomechanical evolution of ductile complex. *Tectonics*, **16,** 983–1000.

Dunlap, W.J., Weinberg, R.F. & Searle, M.P., 1998. Karakoram fault zone rocks cool in two phases. *Journal of the Geological Society*, **155,** 903–912.

Festa, V., 2009. *C*-axis fabrics of quartz-ribbons during high-temperature deformation of syn-tectonic granitoids (Sila Massif, Calabria, Italy). *Comptes Rendus Geosciences*, **341,** 557–567.

Flood, R.H. & Vernon, R.H., 1988. Microstructural evidence of orders of crystallization in granitoid rocks. *Lithos*, **21,** 237–245.

Franěk, J., Schulmann, K., Lexa, O. *et al*., 2011. Origin of felsic granulite microstructure by heterogeneous decomposition of alkali feldspar and extreme weakening of orogenic lower crust during the Variscan orogeny. *Journal of Metamorphic Geology*, **29,** 103–130.

Gagnevin, D., Daly, J.S. & Poli, G., 2004. Petrographic, geochemical and isotopic constraints on magma dynamics and mixing in the Miocene Monte Capanne monzogranite (Elba Island, Italy). *Lithos*, **78,** 157–195.

Gapais, D. & Barbarin, B., 1986. Quartz fabric transition in a cooling syntectonic granite (Hermitage Massif, France). *Tectonophysics*, **125,** 357–370.

Gardien, V., Thompson, A.B. & Ulmer, P., 2000. Melting of biotite + plagioclase + quartz gneisses: the role of H_2O in the stability of amphibole. *Journal of Petrology*, **41,** 651–666.

Gleason, G.C., Tullis, J. & Heidelbach, F., 1993. The role of dynamic recrystallization in the development of lattice preferred orientations in experimentally deformed quartz aggregates. *Journal of Structural Geology*, **15,** 1145–1168.

Green, H.W., 1967. Quartz: extreme preferred orientation produced by annealing. *Science*, **157,** 1444–1447.

Green, N.L., 1994. Mechanism for middle to upper crustal contamination: evidence from continental margin magmas. *Geology*, **22,** 231–234.

Grove, T.L., Kinzler, R.J., Baker, M.B., Donnelly-Nolan, J.M. & Lesher, C.E., 1988. Assimilation of granite by basaltic magma at Burnt Lava flow, Medicine Lake volcano, northern California: decoupling of heat and mass transfer. *Contributions to Mineralogy and Petrology*, **99,** 320–343.

Hasalová, P., Schulmann, K., Lexa, O. *et al*., 2008. Origin of migmatites by deformation-enhanced melt infiltration of orthogneiss: a new model based on quantitative microstructural analysis. *Journal of Metamorphic Geology*, **26,** 29–53.

Heilbronner, R. & Tullis, J., 2002. The effect of static annealing on microstructures and crystallographic preferred orientations of quartzites experimentally deformed in axial compression and shear. *Geological Society, London, Special Publications*, **200,** 191–218.

Hibbard, M.J., 1965. Origin of some feldspar phenocrysts and their bearing on petrogenesis. *American Journal of Science*, **263,** 245–261.

Hibbard, M.J., 1981. The magma mixing origin of mantled feldspars. *Contributions to Mineralogy and Petrology*, **76,** 158–170.

Hibbard, M.J., 1987. Deformation of incompletely crystallized magma systems: granitic gneisses and their tectonic implications. *Journal of Geology*, **95,** 543–561.

Higgins, M.W., 1971. Cataclastic rocks. United States Geological Survey Professional Paper 687, 97 p.

Holness, M.D. & Sawyer, E., 2008. On the pseudomorphing of melt-filled pores during the crystallization of migmatites. *Journal of Petrology*, **49,** 1343–1363.

Humphreys, F.J. & Hatherly, M., 1996. *Recrystallization and Related Annealing Phenomena*. Elsevier, Oxford.

Huppert, H.E. & Sparks, R.S.J., 1988. The generation of granitic magmas by intrusion of basalt into continental crust. *Journal of Petrology*, **29,** 599–624.

Jessell, M.W., 1987. Grain-boundary migration microstructures in naturally deformed quartzite. *Journal of Structural Geology*, **9,** 1007–1014.

Jurewitz, S.R. & Watson, E.B., 1984. Distribution of partial melt in a felsic system: the importance of surface energy. *Contributions to Mineralogy and Petrology*, **85,** 25–29.

Kerr, A. & Fryer, B.J., 1993. Nd isotope evidence for crust-mantle interaction in the generation of A-type granitoid suites in Labrador, Canada. *Chemical Geology*, **104,** 39–60.

Kerr, A.C., Kempton, P.D. & Thompson, R.N., 1995. Crustal assimilation during turbulent magma ascent (ATA); New isotopic evidence from the Mull Tertiary lava succession. *Contributions to Mineralogy and Petrology*, **119,** 142–154.

Kistler, R.W., 1974. Phanerozoic batholiths in western North America; a summary of some recent work on variations in time, space, chemistry, and isotopic compositions. *Annual Review of Earth and Planetary Sciences*, **2,** 403–417.

Kretz, R., 1983. Symbols for rock-forming minerals. *American Mineralogist*, **68,** 277–279.

Lacassin, R., Valli, F., Arnaud, N. *et al*., 2004. Large-scale geometry, offset and kinematic evolution of the Karakorum fault, Tibet. *Earth and Planetary Science Letters*, **219,** 255–269.

Laporte, D., Rapaille, C. & Provost, A., 1997. Wetting angle, equilibrium melt geometry, and the permeability threshold of partially molten crustal protoliths. In: *Granite: From Segregation of Melt to Emplacement Fabrics* (eds Bouchez, J.L.,

Hutton, D.H.W. & Stephens, W.E.), pp. 31–54. Kluwer, Dordrecht.
Leeman, W.P., Vicenzi, E.P., MacRae, C.M., Wilson, N.C., Torpy, A. & Lee, C.A., 2008. Systematics of cathodoluminescence and trace element compositional zoning in natural quartz from volcanic rocks: Ti mapping in quartz. *Microscopy and Microanalysis*, **14,** S2.
MacRae, C.M. & Wilson, N.C., 2008. Luminescence database I – minerals and materials. *Microscopy and Microanalysis*, **14,** 184–204.
MacRae, C.M., Wilson, N.C., Johnson, S.E., Phillips, P.L. & Otsuki, M., 2005. Hyperspectral mapping – combining cathodoluminescence and X-ray collection in an electron microprobe. *Microscopy Research and Technique*, **67,** 271–277.
Mahéo, G., Blichert-Toft, J., Pin, C., Guillot, S. & Pêcher, A., 2009. Partial melting of mantle and crustal sources beneath South Karakorum, Pakistan: implications for the Miocene geodynamic evolution of the India–Asia convergence zone. *Journal of Petrology*, **50,** 427–449.
Mainprice, D., Bouchez, J.L., Blumenfeld, P. & Tubia, J.M., 1986. Dominant *c*-slip in naturally deformed quartz: implications for dramatic plastic softening at high temperature. *Geology*, **14,** 812–822.
Mancktelow, N.S. & Pennacchioni, G., 2004. The influence of grain boundary fluids on the microstructure of quartz-feldspar mylonites. *Journal of Structural Geology*, **26,** 47–69.
Marchildon, N. & Brown, M., 2001. Melt segregation in late syntectonic anatectic migmatites: an example from the Onawa Contact Aureole, Maine, USA. *Physics and Chemistry of the Earth*, **26,** 225–229.
Marchildon, N. & Brown, M., 2002. Grain-scale melt distribution in two contact aureole rocks: implications for controls on melt localization and deformation. *Journal of Metamorphic Geology*, **20,** 381–396.
Marchildon, N. & Brown, M., 2003. Spatial distribution of melt-bearing structures in anatectic rocks from Southern Brittany, France: implications for melt transfer at grain- to orogen-scale. *Tectonophysics*, **364,** 215–235.
McCarthy, M.R. & Weinberg, R.F., 2010. Structural complexity resulting from pervasive ductile deformation in the Karakoram Shear Zone, Ladakh, NW India. *Tectonics*, **29,** TC3004.
McLellan, E.L., 1983. Contrasting textures in metamorphic and anatectic migmatites – an example from the Scottish Caledonides. *Journal of Metamorphic Geology*, **1,** 241–262.
Means, W.D., 1989. Synkinematic microscopy of transparent polycrystals. *Journal of Structural Geology*, **11,** 163–174.
Mehnert, K.R., Büsch, W. & Schneider, G., 1973. Initial melting at grain boundary of quartz and feldspar in gneisses and granulites. *Neues Jahrbuch Für Mineralogie Monatshefte*, **4,** 165–183.
Miller, R.B. & Paterson, S.R., 1994. The transition from magmatic to high-temperature solid-state deformation: implications from the Mount Stuart batholith, Washington. *Journal of Structural Geology*, **16,** 853–865.
Mogk, D.W., 1992. Ductile shearing and migmatization at mid-crustal levels in an Archaean high-grade gneiss belt, northern Gallatin Range, Montana, USA. *Journal of Metamorphic Geology*, **10,** 427–438.
Nyman, M.W., Law, R.D. & Smelik, E.A., 1992. Cataclastic deformation mechanism for the development of core-mantle structures in amphibole. *Geology*, **20,** 455–458.
Oliot, E., Goncalves, P. & Marquer, D., 2010. Role of plagioclase and reaction softening in a metagranite shear zone at mid crustal conditions (Gotthard Massif, Swiss Central Alps). *Journal of Metamorphic Geology*, **28,** 849–871.
Otani, M. & Wallis, S., 2006. Quartz lattice preferred orientation patterns and static recrystallization: natural examples from the Ryoke belt, Japan. *Geology*, **34,** 561–564.
Park, Y. & Means, W.D., 1996. Direct observation of deformational processes in crystal mushes. *Journal of Structural Geology*, **18,** 847–858.
Parrish, R.R. & Tirrul, R., 1989. U-Pb age of the Baltoro granite, northwest Himalaya, and implications for monazite U-Pb systematics. *Geology*, **17,** 1076–1079.
Passchier, C.W. & Trouw, R.A.J., 1996. *Microtectonics*. Springer-Verlag, Berlin, Heidelberg.
Paterson, S.R., Vernon, R.H. & Tobish, O.T., 1989. A review of criteria for the identification of magmatic and tectonic foliations in granitoids. *Journal of Structural Geology*, **11,** 349–363.
Peternell, M., Kohlmann, F., Wilson, C.J.L., Seiler, C. & Gleadow, A.J.W., 2009. A new approach to crystallographic orientation measurement for apatite fission track analysis: effects of crystal morphology and implications for automation. *Chemical Geology*, **265,** 527–539.
Peternell, M., Hasalová, P., Wilson, C.J.L., Piazolo, S. & Schulmann, K., 2010. Evaluating quartz crystallographic preferred orientations and the role of deformation partitioning using EBSD and fabric analyser techniques. *Journal of Structural Geology*, **32,** 803–812.
Phillips, R.J., Parrish, R.R. & Searle, M.P., 2004. Age constraints on ductile deformation and long-term slip rates along the Karakoram fault zone, Ladakh. *Earth and Planetary Science Letters*, **226,** 305–319.
Poli, G., 1992. Geochemistry of Tuscan Archipelago Granitoids, central Italy: the role of hybridization processes in their genesis. *Journal of Geology*, **100,** 41–56.
Ravikant, V., 2006. Utility of Rb-Sr geochronology in constraining Miocene and Cretaceous events in the eastern Karakoram, Ladakh, India. *Journal of Asian Earth Sciences*, **27,** 534–543.
Ree, J.H. & Park, Y., 1997. Static recovery and recrystallization microstructures in sheared octachloropropane. *Journal of Structural Geology*, **19,** 152–1526.
Reichardt, H. & Weinberg, R.F., in press. The dike swarm of the Karakoram Shear Zone, Ladakh, NW India: linking source to batholith. *Geological Society of America Bulletin*, doi: 10.1130/B30394.1.
Reichardt, H., Weinberg, R.F., Andersson, U.B. & Fanning, M.C., 2010. Hybridization of granitic magmas in the source: the origin of the Karakoram Batholith, Ladakh, NW India. *Lithos*, **116,** 249–272.
Reid, J.B., Ewans, O.C. & Fates, D.G., 1983. Magma mixing in granitic rocks of the central Sierra Nevada, California. *Earth and Planetary Science Letters*, **66,** 243–261.
Reiners, P.W., Nelson, B.K. & Ghiorso, M.S., 1995. Assimilation of felsic crust by basaltic magma: Thermal limits and extents of crustal contamination of mantle-derived magmas. *Geology*, **23,** 563–566.
Rolland, Y. & Pêcher, A., 2001. The Pangong granulites of the Karakoram Fault (western Tibet); vertical extrusion within a lithosphere-scale fault? *Comptes Rendus de l'Academie des Sciences, Serie II. Sciences de la Terre et des Planetes*, **332,** 363–370.
Rolland, Y., Mahéo, G., Pêcher, A. & Villa, I.M., 2009. Synkinematic emplacement of the Pangong metamorphic and magmatic complex along the Karakorum Fault (N Ladakh). *Journal of Asian Earth Sciences*, **34,** 10–25.
Rosenberg, C.L. & Handy, M.R., 2005. Experimental deformation of partially melted granite revisited: implications for the continental crust. *Journal of Metamorphic Geology*, **23,** 19–28.
Rosenberg, C.L. & Riller, U., 2000. Partial-melt topology in statically and dynamically recrystallized granite. *Geology*, **28,** 7–10.
Rusk, B., Reed, M., Dilles, J. & Kent, A., 2006. Intensity of quartz cathodoluminescence and trace element content of quartz from the porphyry copper deposit in Butte, Montana. *American Mineralogist*, **91,** 1300–1312.
Rutter, E.H., Faulkner, D.R., Brodie, K.H., Phillips, R.J. & Searle, M.P., 2007. Rock deformation processes in the Karakoram fault zone, Eastern Karakoram, Ladakh, NW India. *Journal of Structural Geology*, **29,** 1315–1326.

de Saint Blanquat, M. & Tikoff, B., 1997. Development of magmatic to solid-state fabrics during syntectonic emplacement of the Mono Creek granite, Sierra Nevada Batholith, California. In: *Granite: from Melt Segregation to Emplacement Fabrics* (eds Bouchez, J.L., Stephens, W.E. & Hutton, D.E.), pp. 231–252. Kluwer, Dordrecht.

Sander, B., 1950. *Einfuehrung in die Gefuegekunde der Geologischen Koerper; Zweiter Teil, Die Korngefuege*. Springer-Verlag, Wien-Innsbruck.

Sawyer, E.W., 1999. Criteria for the recognition of partial melting. *Physics and Chemistry of the Earth*, **24,** 269–279.

Sawyer, E.W., 2001. Melt segregation in the continental crust: distribution and movement of melt in anatectic rocks. *Journal of Metamorphic Geology*, **19,** 291–309.

Schmid, S.M. & Casey, M., 1986. Complete fabric analysis of some commonly observed quartz [c]-axis patterns. In: *Mineral and Rock Deformation: Laboratory Studies* (eds Hobbs, B.E. & Heard, H.C.), pp. 263–288. American Geophysical Union, Geophysical Monographs, Washington D.C.

Schulmann, K., Edel, J.B., Hasalová, P., Cosgrove, J.W., Ježek, J. & Lexa, O., 2009. Influence of melt induced mechanical anisotropy on the magnetic fabrics and rheology of deforming migmatites, Central Vosges, France. *Journal of Structural Geology*, **31,** 1223–1237.

Searle, M.P. & Phillips, R.J., 2007. Relationships between right-lateral shear along the Karakoram fault and metamorphism, magmatism, exhumation and uplift: evidence from the K2-Gasherbrum-Pangong ranges, north Pakistan and Ladakh. *Journal of the Geological Society*, **164,** 439–450.

Searle, M.P., Weinberg, R.F. & Dunlap, W.J., 1998. Transpressional tectonics along the Karakoram fault zone, northern Ladakh: constraints on Tibetan extrusion. In: *Continental Transpressional and Transpressional Tectonics* (eds Holdsworth, R.E., Strachan, R.A.S. & Dewey, J.F.), Vol. 135, pp. 307–326. Geological Society, London, Special Publications.

Slagstad, T., Jamieson, R.A. & Culshaw, N.G., 2005. Formation, crystallization, and migration of melt in the mid-orogenic crust: Muskoka Domain Migmatites, Grenville Province, Ontario. *Journal of Petrology*, **46,** 893–919.

Soesoo, A. & Nicholls, I.A., 1999. Mafic rocks spatially associated with Devonian felsic intrusions of the Lachlan Fold Belt: a possible mantle contribution to crustal evolution processes. *Australian Journal of Earth Sciences*, **46,** 725–734.

Spear, F.S. & Wark, D.A., 2009. Cathodoluminescence imaging and titanium thermometry in metamorphic quartz. *Journal of Metamorphic Geology*, **27,** 187–205.

Srimal, N., 1986. India-Asia collision: implications from the geology of the eastern Karakoram. *Geology*, **14,** 523–527.

Stipp, M., Stünitz, H., Heilbronner, R. & Schmid, S.M., 2002. The eastern Tonale fault zone: a 'natural laboratory' for crystal plastic deformation of quartz over a temperature range from 250 to 700 °C. *Journal of Structural Geology*, **24,** 1861–1884.

Stöckhert, B. & Duyster, J., 1999. Discontinuous grain growth in recrystallised vein quartz – implications for grain boundary structure, grain boundary mobility, crystallographic preferred orientation, and stress history. *Journal of Structural Geology*, **21,** 1477–1490.

Stünitz, H., 1998. Syndeformational recrystallization – dynamic or compositionally induced? *Contributions to Mineralogy and Petrology*, **131,** 219–236.

Thomas, J.B., Watson, E.B., Spear, F.S., Shemella, P.T., Nayok, S.K. & Lanzirotti, A., 2010. TitaniQ under pressure: the effect of pressure and temperature on the solubility of Ti in quartz. *Contributions to Mineralogy and Petrology*, **160,** 743–759.

Thompson, A.B., 1982. Dehydration melting of pelitic rocks and the generation of H_2O-undersaturated granitic liquids. *American Journal of Science*, **282,** 1567–1595.

Tullis, J. & Yund, R.A., 1985. Dynamic recrystallization of feldspar: a mechanism of ductile shear zone formation. *Geology*, **15,** 238–241.

Tullis, J., Christie, J.M. & Griggs, D.T., 1973. Microstructures and preferred orientations of experimentally deformed quartzites. *Geological Society of America Bulletin*, **84,** 297–314.

Vernon, R.H., 1990. K-feldspar augen in felsic gneisses and mylonites – deformed phenocrysts or porphyroblasts? *Journal of the Geological Society of Sweden*, **112,** 157–167.

Vernon, R.H., 1991. Questions about myrmekite in deformed rocks. *Journal of Structural Geology*, **13,** 979–985.

Vernon, R.H., 1999. Quartz and feldspar microstructures in metamorphic rocks. *Canadian Mineralogist*, **37,** 513–524.

Vernon, R.H., 2000. Review of microstructural evidence of magmatic and solid-state flow. *Electronic Geosciences*, **5,** 2.

Vernon, R.H., 2004. *A Practical Guide to Rock Microstructures*. Cambridge University Press, Cambridge.

Vernon, R.H. & Paterson, S.R., 2001. Axial-surface leucosomes in anatectic migmatites. *Tectonophysics*, **335,** 183–192.

Vernon, R.H., Johnson, S.E. & Melis, E.A., 2004. Emplacement-related microstructures in the margin of a deformed pluton: the San José tonalite, Baja California, México. *Journal of Structural Geology*, **26,** 1867–1884.

Vidal, J.L., Kubin, L., Debat, P. & Soula, J.C., 1980. Deformation and dynamic recrystallization of K-feldspar augen in orthogneiss from Montagne Noire, Occitania, Southern France. *Lithos*, **13,** 247–255.

Wark, D.A. & Spear, F.S., 2005. Titanium in quartz: cathodoluminescence and thermometry. *Geochimica et Cosmochimica Acta*, **69,** A592.

Wark, D.A. & Watson, E.B., 2006. TitaniQ: a titanium-in-quartz geothermometer. *Contributions to Mineralogy and Petrology*, **152,** 743–754.

Wark, D.A., Hildreth, W., Spear, F.S., Cherniak, D.J. & Watson, E.B., 2007. Pre-eruption recharge of the Bishop magma system. *Geology*, **35,** 235–238.

Weinberg, R.F. & Mark, G., 2008. Magma migration, folding, and disaggregation of migmatites in the Karakoram Shear Zone, Ladakh, NW India. *Geological Society of America Bulletin*, **120,** 994–1009.

Weinberg, R.F. & Regenauer-Lieb, K., 2010. Ductile fractures and magma migration from source. *Geology*, **38,** 363–366.

Weinberg, R.F. & Searle, M.P., 1998. The Pangong Injection Complex, Indian Karakoram: a case of pervasive granite flow through hot viscous crust. *Journal of Geological Society*, **155,** 883–891.

Weinberg, R.F., Dunlap, W.J. & Whitehouse, M., 2000. New field, structural and geochronological data from the Shyok and Nubra Valleys, northern Ladakh: linking Kohistan to Tibet. In: *Tectonics of the Nanga Parbat Syntaxis and the Western Himalaya* (eds Khan, M.A., Treloar, P.J., Searle, M.P. & Jan, M.Q.), Vol. 170, pp. 253–275. Geological Society, London, Special Publications.

Weinberg, R.F., Mark, G. & Reichardt, H., 2009. Magma ponding in the Karakoram shear zone, Ladakh, NW India. *Geological Society of America Bulletin*, **121,** 278–285.

White, R.W., Powell, R. & Holland, T.J.B., 2007. Progress relating to calculation of partial melting equilibria for metapelites. *Journal of Metamorphic Geology*, **25,** 511–527.

Wiebe, R.A., Wark, D.A. & Hawkins, D.P., 2007. Insights from quartz cathodoluminescence zoning into crystallization of the Vinalhaven granite, coastal Maine. *Contributions to Mineralogy and Petrology*, **154,** 439–453.

Wilson, C.J.L., Russell-Head, D.S. & Sim, H.M., 2003. The application of an automated fabric analyser system to the textural evolution of folded ice layers in shear zones. *Annals of Glaciology*, **37,** 7–17.

Wilson, C.J.L., Russell-Head, D.S., Kunze, K. & Viola, G., 2007. The analysis of quartz *c*-axis fabrics using a modified optical microscope. *Journal of Microscopy*, **227,** 30–41.

Received 16 November 2010; revision accepted 26 April 2011.